

# Understanding catalytic CO<sub>2</sub> and CO conversion into methanol using computational fluid dynamics

## Electronic Supplementary Information

Stylianos Kyrimis, Matthew E. Potter, Robert Raja, and Lindsay-Marie Armstrong

### Contents

<b>Geometry and Mesh setup</b> .....	3
<b>Modelling Methodology</b> .....	3
<b>Conservation equations</b> .....	3
<b>Porous medium formulation</b> .....	4
<b>Diffusion transfer and Dusty-gas model implementation</b> .....	4
<b>Reaction kinetic constants</b> .....	5
<b>Boundary conditions</b> .....	6
<b>Solution setup</b> .....	7
<b>Simulation Results</b> .....	7
<b>Model Validation</b> .....	7
<b>Feed 13</b> .....	8
<b>Feed 14</b> .....	11
<b>Feed 15</b> .....	15
<b>Feed 23</b> .....	20
<b>Feed 25</b> .....	23
<b>Grid dependency study</b> .....	27
<b>Feed 23</b> .....	27
<b>Feed 13</b> .....	30
<b>Backflow significance</b> .....	33
<b>References</b> .....	34

<i>Nomenclature</i>	
$d_p$	Catalytic particle diameter, [m]
$Deff,i$	Effective diffusion coefficient of species $i$ , [m <sup>2</sup> /sec]
$\mathcal{D}_{ij}$	Binary diffusion coefficient between species $i$ and $j$ , [m <sup>2</sup> /sec]
$D_{Kn,i}$	Knudsen diffusion coefficient of species $i$ , [m <sup>2</sup> /sec]
$d_{pore}$	Pore diameter, [m]
$D_r$	Reactor diameter, [m]
$\vec{g}$	Gravitational acceleration, [m/s <sup>2</sup> ]
$h_i$	Enthalpy of species $i$ , [J/kmol]
$\vec{J}_i$	Diffusive flux of species $i$ , [kg/(m <sup>2</sup> ·sec)]
$K_{eq,i}$	Equilibrium constant of reaction $i$
$k_{eff}$	Effective thermal conductivity, [W/(m·K)]
$M_{w,i}$	Molecular weight of species $i$ , [kg/kmol]
$N_i$	Molar flux of species $i$ , [kmol/(m <sup>2</sup> ·sec)]
$P$	Pressure, [Pa]
$r_i$	Reaction rate based on the respective kinetic model, [kmol/(m <sup>3</sup> ·sec)]
$R_i$	Reaction source term, [kg/(m <sup>3</sup> ·sec)]
$T$	Temperature, [K]
$\vec{u}$	Superficial velocity, [m/sec]
$v_i$	Atomic diffusion volume of species $i$
$v_{i,r}^{prod}$	Stoichiometric coefficient of product species $i$ in reaction $r$
$v_{i,r}^{react}$	Stoichiometric coefficient of reactant species $i$ in reaction $r$
$X_i$	Molar fraction of species $i$
$Y_i$	Mass fraction of species $i$
<i>Greek letters</i>	
$\varepsilon_{Bulk}$	Bulk porosity of fixed bed
$\tau_{porous}$	Tortuosity of fixed bed
$\rho$	Density, [kg/m <sup>3</sup> ]
$\bar{\tau}$	Stress tensor, [kg/(m·sec <sup>2</sup> )]
$\varphi^i$	Scalar quantity of species $i$

## Geometry and Mesh setup

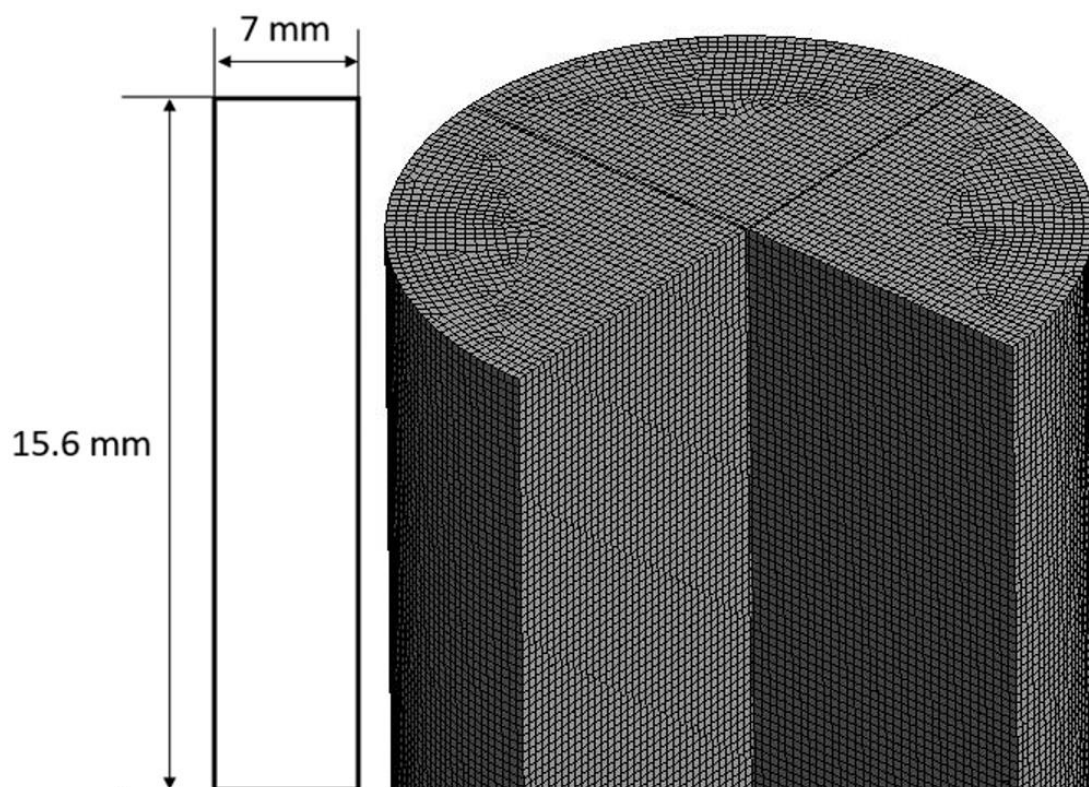


Figure A 1: Geometry schematic and mesh setup, based on the experimental data of Park et al. (1).

## Modelling Methodology

### Conservation equations

The Ansys® Academic Research, Release 2019 R2, simulation software was used for this study, with Fluent as the computational code. As a steady-state simulation is considered, Fluent solves the following conservation equations of mass, Eq. ( 1 ), momentum, Eq. ( 2 ), and energy, Eq. ( 3 ), to predict the flow profile and transfer of species within each computational elements (2, 3):

$$\nabla(\rho\vec{u}) = 0 \quad (1)$$

$$\nabla(\rho\vec{u}\vec{u}) = -\nabla P + \nabla\bar{\tau} + \rho\vec{g} \quad (2)$$

$$\nabla\left(\vec{u}\left(\rho\left(h - \frac{P}{\rho} + \frac{u^2}{2}\right) + P\right)\right) = \nabla\left(k_{eff}\nabla T - \sum_i h_i\vec{J}_i + (\bar{\tau}\vec{u})\right) + S_h \quad (3)$$

Here, the velocity,  $\vec{u}$ , considered by Fluent within the porous medium is the superficial velocity. This corresponds to the physical velocity that a flow would have within a non-porous domain of the same dimensions, multiplied by the defined porosity of the medium. Using the superficial velocity, the porosity is not taken into account in the convection and diffusion terms of the transport equations (3). Thermal equilibrium is not enforced within the porous medium. The heat release/consumption due to the exo-/endothermicity of the involved reactions,  $R_i$ , is considered through an energy source/sink term,  $S_h$ , in the energy equation.  $S_h$  is estimated from the enthalpy of the consumed and produced species (2), through Eq. ( 4 ).

$$S_h = - \sum_i \frac{h_i}{M_{w,i}} \cdot R_i \quad (4)$$

$$R_i = M_{w,i} \sum_i (v_{i,r}^{prod} - v_{i,r}^{react}) \cdot r_i \quad (5)$$

The species conservation equation, Eq. ( 6 ), normally considered by Fluent (2, 3) along the conservation equations of mass, momentum, and energy, is instead replaced by the conservation equations of the scalar quantities, Eq. ( 8 ).

$$\nabla \cdot (\rho \vec{u} Y_i) + \nabla \cdot \vec{J}_i = R_i \quad (6)$$

$$\vec{J}_i = -\rho D_{i,m} \nabla Y_i - D_{T,i} \frac{\nabla T}{T} \quad (7)$$

$$\nabla \cdot (\rho \vec{u} \varphi^i - \rho D_{eff,i} \nabla \varphi^i) = R_i \quad (8)$$

The two equations are actually identical, and since the mass fractions,  $Y_i$ , of the reactant and the product species are replaced by the respective values of the scalar quantities,  $\varphi^i$ , at the end of each iteration, solving both equations is unnecessary. The term  $\vec{J}_i$  in the species conservation equation, given in Eq. ( 7 ), represents the diffusive flux of species, as a result of concentration and of temperature gradients (Fick's law) (2). It is dependent on the thermal diffusion coefficient,  $D_{T,i}$ , and the bulk diffusion coefficient of species i in mixture m,  $D_{i,m}$ . The latter is taken into account in the scalar conservation equations, as  $D_{eff,i}$ , calculated from the Dusty-Gas diffusion model, presented in a following section, and implemented through User-Defined Functions (UDFs), i.e. external user codes. At the moment, the thermal diffusion coefficient is not implemented in the model. Due to the small temperature gradients estimated from Fluent for the laboratory scale setup of Park *et al.* (1), the contribution of the thermal diffusion coefficient is assumed negligible. For larger scale reactors though, where temperature gradients of around 40 K are possible (4), this term is expected to have a significant contribution in the local diffusion transfer of species.

### Porous medium formulation

The porous medium is defined using a constant volumetric porosity with no near-wall variations. This means that a single porosity value is defined across the entire volume of the porous medium, which was estimated from Eq. ( 9 ), taken from the correlation presented by Achenbach (5).

$$\varepsilon_{Bulk} = 0.78 \left( \frac{d_p}{D_r} \right)^2 + 0.375 \quad (9)$$

The particle diameter,  $d_p$ , used was 0.2 mm, representing the average of the sieve size used experimentally by Park *et al.* (1). Volume blockage within the computational packed bed, due to the existence of the catalytic particles, is not considered by Fluent (3). Instead, the porous medium model of Fluent introduces a momentum sink in the conservation equations to modify the flow characteristics (3). The pressure drop along the axial direction of the catalytic bed,  $\Delta y$ , is estimated from the Ergun equation, as the sum of the Viscous, Eq. ( 10 ), and the Inertial, Eq. ( 11 ), resistances (2).

$$\Delta P_{viscous} = \frac{150(1 - \varepsilon_{Bulk})^2}{d_p^2 \varepsilon_{Bulk}^3} \mu u \Delta y \quad (10)$$

$$\Delta P_{inertial} = \frac{3.5(1 - \varepsilon_{Bulk}) \rho}{d_p \varepsilon_{Bulk}^3} \frac{\rho}{2} u^2 \Delta y \quad (11)$$

### Diffusion transfer and Dusty-gas model implementation

Fluent's user-interface (UI) does not directly allow the combination of Bulk and of Knudsen diffusivities in its diffusivity model. Dixon *et al.* (6-8) applied the scalar equation theory, available in Fluent, to implement Bulk and Knudsen diffusivity, in the form of the dusty-gas diffusion correlation, in their discrete element CFD model. The dusty-gas model, Eq. ( 12 ), initially introduced by Hite and Jackson

(9), considers the contribution of both bulk (inter-molecular) diffusion, through the binary diffusion coefficient of species (10), Eq. ( 14 ), and Knudsen diffusion (11), Eq. ( 15 ).

$$\frac{1}{D_{eff,i}} = \frac{\sum_j^{N_{sp}} \frac{1}{\Delta_{ij}} \left( Y_j - Y_i \frac{N_j}{N_i} \right)}{1 - Y_i \sum_j^{N_{sp}} \frac{N_j}{N_i}} \quad (12)$$

$$\frac{1}{\Delta_{ij}} = \frac{1}{D_{ij}} + \frac{1}{D_{Kn,i} D_{Kn,j} \sum_m \frac{Y_m}{D_{Kn,m}}} \quad (13)$$

$$D_{ij} = \frac{\varepsilon_{Bulk}}{\tau_{Porous}} \frac{1.43 \cdot 10^{-8} \cdot T^{1.75} \cdot \left( \frac{1}{M_{w,i}} + \frac{1}{M_{w,j}} \right)^{0.5}}{P \cdot \left( \sum v_i^{\frac{1}{3}} + \sum v_j^{\frac{1}{3}} \right)^2} \quad (14)$$

$$D_{Kn,i} = \frac{\varepsilon_{Bulk}}{\tau_{Porous}} \cdot \frac{d_{pore}}{3} \sqrt{\frac{8RT}{\pi M_{w,i}}} \quad (15)$$

In Eq. ( 14 ), the atomic diffusion volumes,  $v_i$  and  $v_j$ , are calculated from Poling et al. (12). The term  $D_{ij}$  is the binary diffusion coefficient and is calculated for each combination of species within the flow mixture. In Eq. ( 15 ),  $d_{pore}$  is assumed to be 20 nm for the commercial catalyst, taken from Graaf *et al.* (13). The term  $\tau_{Porous}$  is the tortuosity of the porous medium, and is equal to 2.59, estimated from Beeckman (14, 15). The term  $D_{Kn,i}$ , Eq. ( 15 ), represents diffusions due to molecule-catalytic wall collisions, as the species flow through the porous network.

In this paper, a similar methodology to Dixon *et al.* (6-8) will be used. As stated earlier, Fluent allows the definition of User-Defined Scalars (UDS) (2). The dusty-gas model is implemented in their conservation equation, Eq. ( 8 ), as  $D_{eff,i}$ , through UDFs. The scalar quantities, depicted as  $\varphi^i$ , represent the mass fractions of the reactants and of the product species. In practise, each  $\varphi^i$  quantity is considered to have the molecular properties, e.g.  $M_{w,i}$ , density, etc., of its respective species, when calculating diffusion transfer or reaction rate terms, e.g.  $D_{ij}$ ,  $D_{Kn,i}$ , etc. The production and destruction of the scalar quantities as a result of the chemical reactions are defined using a source term,  $R_i$ , given in Eq. ( 5 ). Both the dusty-gas diffusion model and the chemical reactions are applied volumetrically and no distinction between intra- and inter- particle space was made.

## Reaction kinetic constants

The reaction rate constants, applied in the reaction rate equations, are presented in Table A 1 and Table A 2, for the kinetic model (KM) of Park and of Nestler, respectively.

Table A 1: Kinetic constant parameters used in Park's KM. The units have been modified accordingly to follow the expected units of Fluent.

Park KM – Ref: (1, 16)		
Const.	Value	Unit
$k_1$	$1.26 \cdot 10^5 \cdot \exp\left(\frac{-6.825 \cdot 10^7}{RT}\right)$	$\frac{kmol}{m_{cat}^3 \cdot s \cdot bar^{1.5}}$
$k_2$	$2.06 \cdot 10^{10} \cdot \exp\left(\frac{-1.266 \cdot 10^8}{RT}\right)$	$\frac{kmol}{m_{cat}^3 \cdot s \cdot bar}$
$k_3$	$3.34 \cdot 10^8 \cdot \exp\left(\frac{-1.137 \cdot 10^8}{RT}\right)$	$\frac{kmol}{m_{cat}^3 \cdot s \cdot bar^{1.5}}$

$K_{CO_2}$	$1.02 \cdot 10^{-7} \cdot \exp\left(\frac{6.744 \cdot 10^7}{RT}\right)$	$bar^{-1}$
$K_{CO}$	$8.00 \cdot 10^{-7} \cdot \exp\left(\frac{5.802 \cdot 10^7}{RT}\right)$	$bar^{-1}$
$K_{H_2}$	$27.1 \cdot \exp\left(\frac{-6.291 \cdot 10^6}{RT}\right)$	$bar^{-1}$
$K_{H_2O}$	$3.8 \cdot 10^{-11} \cdot \exp\left(\frac{8.088 \cdot 10^7}{RT}\right)$	$bar^{-1}$

Table A 2: Kinetic constant parameters used in Nestler's KM. The units have been modified accordingly to follow the expected units of Fluent.

Nestler KM – Ref: (4)		
Const.	Value	Unit
$k_1$	$96.045 \cdot \exp\left(\frac{-4.55 \cdot 10^7}{RT}\right)$	$\frac{kmol}{m_{cat}^3 \cdot s \cdot bar}$
$k_2$	$1.39 \cdot 10^4 \cdot \exp\left(\frac{-5.5 \cdot 10^7}{RT}\right)$	$\frac{kmol}{m_{cat}^3 \cdot s \cdot bar^{0.5}}$
$K_1$	$3.32 \cdot 10^{-13} \cdot \exp\left(\frac{1.1 \cdot 10^8}{RT}\right)$	$bar^{-1}$
$K_2$	0.8262	$bar^{-1}$
$K_3$	$2.03 \cdot 10^{-11} \cdot \exp\left(\frac{1.19 \cdot 10^8}{RT}\right)$	$bar^{-0.5}$

The chemical equilibrium constants for the reaction rates,  $K_{eq,1}$ ,  $K_{eq,2}$ , and  $K_{eq,3}$ , are taken from Graaf and Winkelman (2016) (17). They are estimated from Eq. ( 16 )-( 18 ), respectively.

$$K_{eq,1} = K_{eq,2} \cdot K_{eq,3} \quad (16)$$

$$\ln K_{eq,2} = \frac{1}{RT} [-3.94 \cdot 10^4 - 54.2 \cdot T - 5.56 \cdot 10^{-2} \cdot T^2 + 2.58 \cdot 10^{-5} \cdot T^3 - 7.66 \cdot 10^{-9} \cdot T^4 + 1.02 \cdot 10^{-12} \cdot T^5 + 18.43 \cdot T \cdot \ln T] \quad (17)$$

$$\ln K_{eq,3} = \frac{1}{RT} [7.44 \cdot 10^4 + 1.89 \cdot 10^2 \cdot T + 3.24 \cdot 10^{-2} \cdot T^2 + 7.04 \cdot 10^{-6} \cdot T^3 - 5.61 \cdot 10^{-9} \cdot T^4 + 1.03 \cdot 10^{-12} \cdot T^5 - 64.36 \cdot T \cdot \ln T] \quad (18)$$

### Boundary conditions

A mass flow inlet was defined at the top of the porous medium domain. The mass flow rate was estimated from the experimental flow rate, 8000 mL/(g<sub>cat</sub>·h), based on the composition of each different feed, i.e. the mass fractions of the different species. A pressure outlet was specified at the bottom of the porous medium, with a specified target flow rate equal to the inlet flow rate. The reactor walls were defined using no slip-boundary conditions. A constant temperature, equal to the operating temperature in the experimental setup, i.e. 523 K, is assumed in the reactor walls. The operating pressure of the gas mixture is set to 50 bar.

## Solution setup

The pressure-based solver is used, with the SIMPLE algorithm defining the relationship between pressure and velocity (2). This method solves a pressure equation to define the velocity field, derived from the continuity and the momentum equations in such a way that the mass conservation equation is satisfied (2). Second-order discretization scheme was considered for the pressure, the momentum, the energy, and the scalar quantities (3). In addition, the under-relaxation factors were reduced to 0.5 for the pressure and for the momentum, and to 0.3 for the scalar quantities. The solution took roughly 800 iterations to converge.

## Simulation Results

### Model Validation

The expected outlet mass fractions of CO<sub>2</sub> and CO, based on their experimental conversions presented by Park *et al.* (1), are presented in Table A 3 and Table A 4, respectively. In addition, the predicted CO<sub>2</sub> and CO mass fractions from the two kinetic models are also presented, along with their respective relative errors.

Table A 3: Expected outlet mass fractions of CO<sub>2</sub>, based on the experimental conversions of Park *et al.* (1), and predicted mass fractions, along with their respective relative errors, from the two kinetic models.

Feed Number	Expected outlet CO <sub>2</sub> mass fractions [-]	Park's KM		Nestler's KM	
		Predicted CO <sub>2</sub> mass fraction [-]	CO <sub>2</sub> relative error [%]	Predicted CO <sub>2</sub> mass fraction [-]	CO <sub>2</sub> relative error [%]
13	0.595	0.589	1.02	0.589	0.97
14	0.467	0.464	0.34	0.465	0.09
15	0.345	0.346	-0.75	0.347	-1.11
23	0.307	0.304	1.08	0.305	0.71
25	0.247	0.226	8.14	0.227	7.92
Average Error [%]			2.27	2.16	

Table A 4: Expected outlet mass fractions of CO, based on the experimental conversions of Park *et al.* (1), and predicted mass fractions, along with their respective relative errors, from the two kinetic models.

Feed Number	Expected outlet CO mass fractions [-]	Park's KM		Nestler's KM	
		Predicted CO mass fraction [-]	CO relative error [%]	Predicted CO mass fraction [-]	CO relative error [%]
14	0.108	0.107	1.37	0.104	3.69
15	0.174	0.169	2.86	0.160	7.91
23	0.159	0.161	-1.23	0.153	3.84
25	0.100	0.106	-5.35	0.104	-3.86
Average Error [%]			2.7	4.83	

## Feed 13

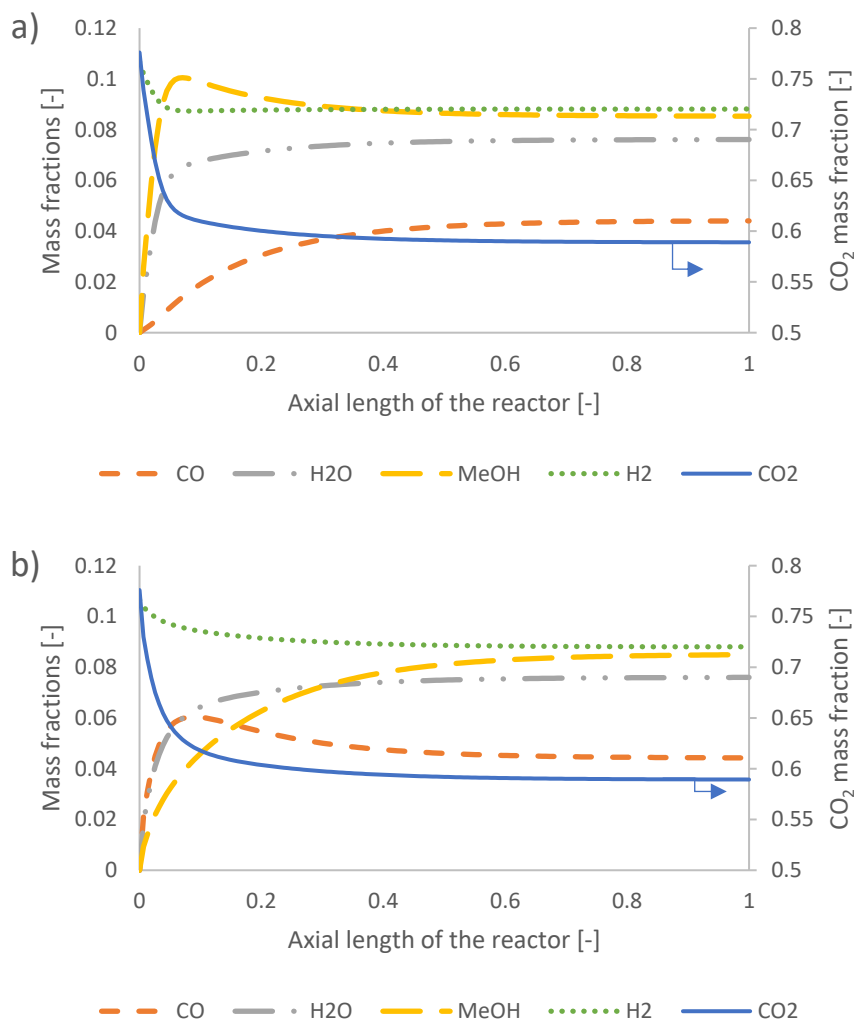


Figure A 2: Mass fractions of species along the axial direction (centreline) of the reactor for feed 13, predicted from a) Park's KM and b) Nestler's KM.

Table A 5: Outlet species mass fractions for feed 13, predicted from the two kinetic models.

Feed 13 Species	Species outlet mass fractions	
	Park's KM	Nestler's KM
CO <sub>2</sub>	0.589	0.589
CO	0.044	0.044
H <sub>2</sub>	0.088	0.088
H <sub>2</sub> O	0.076	0.076
MeOH	0.085	0.085

The local temperature variation corresponds to the local temperature of the computational element minus the operating temperature, equal to 523 K.

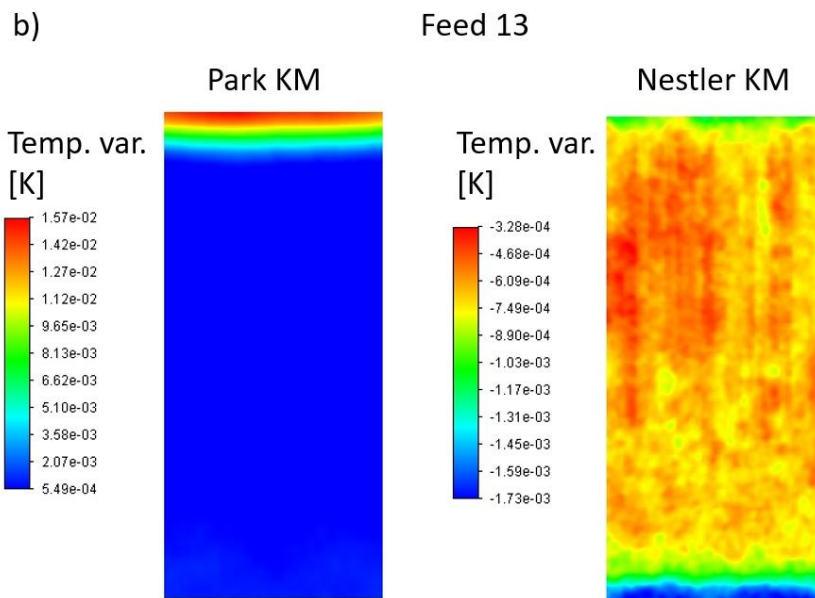
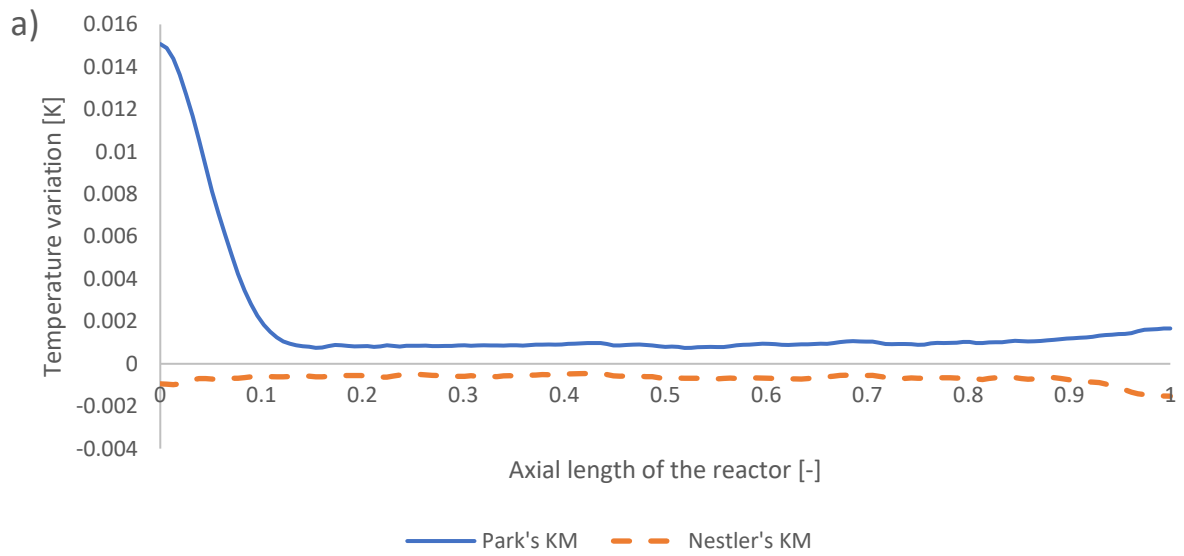


Figure A 3: Local temperature variation a) in the centreline of the reactor, and b) in a 2D plane surface in the centre of the reactor, for feed 13, as predicted from the two KMs.

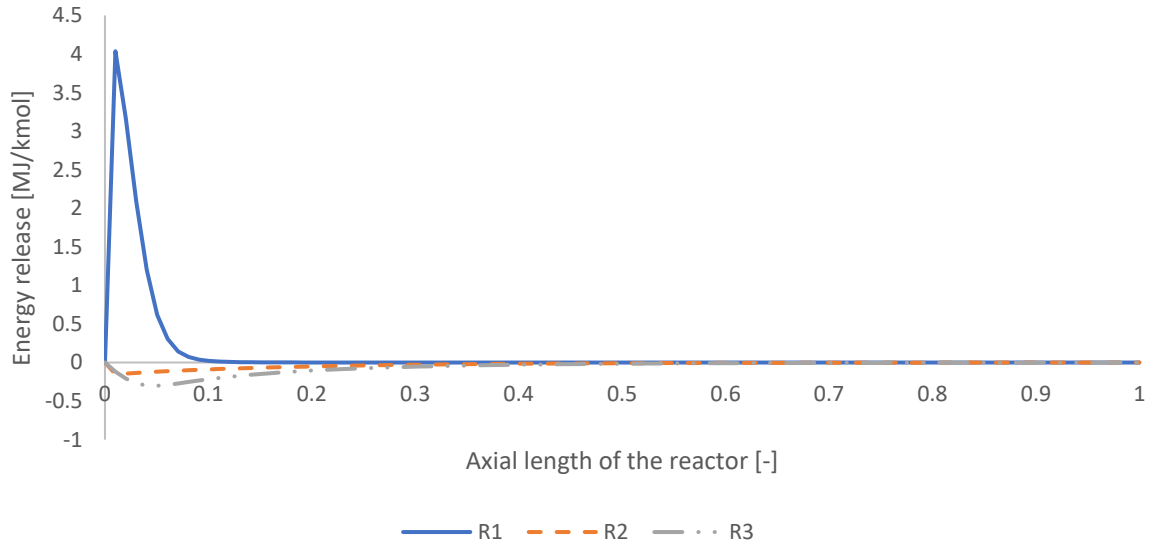


Figure A 4: Energy source or sink of reactions  $R_1$ ,  $R_2$ , and  $R_3$ , as predicted from Park's KM for feed 13.

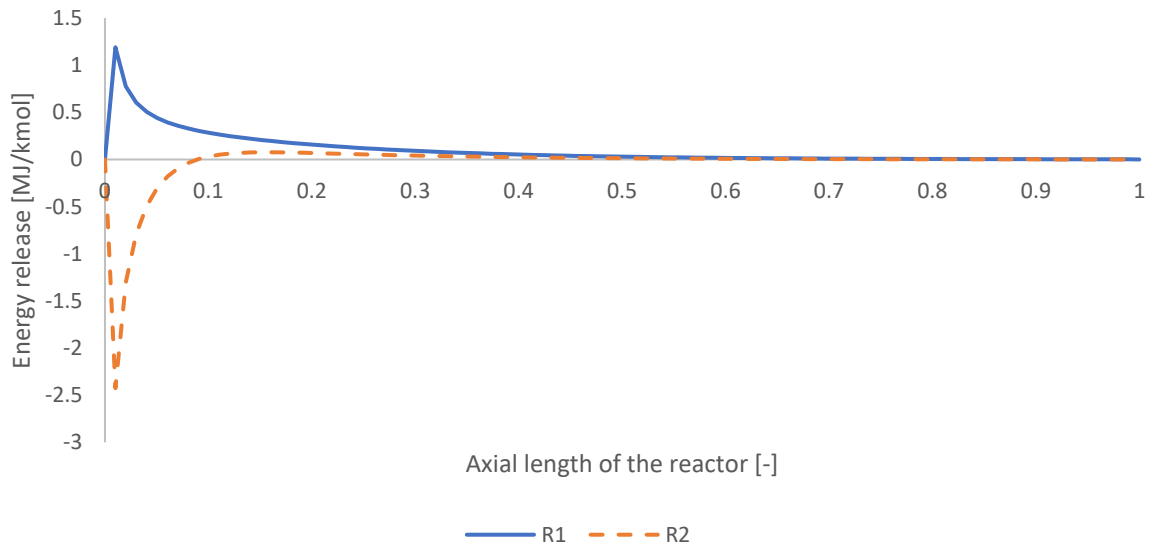


Figure A 5: Energy source or sink of reactions  $R_1$  and  $R_2$ , as predicted from Nestler's KM for feed 13.

## Feed 14

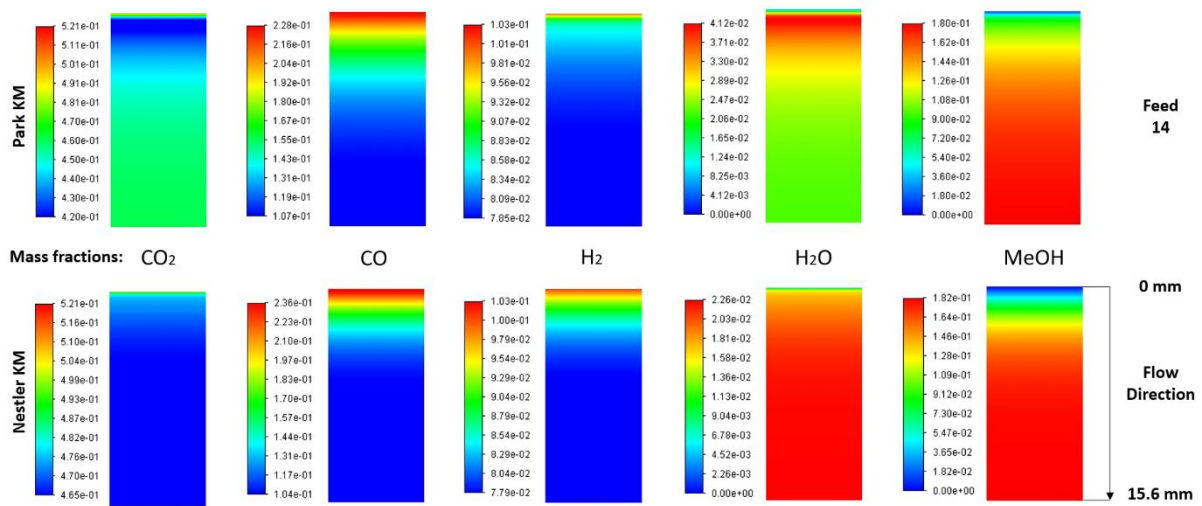


Figure A 6: Mass fractions of species along a 2D plane surface in the centre of the reactor for feed 14, predicted from both KMs.

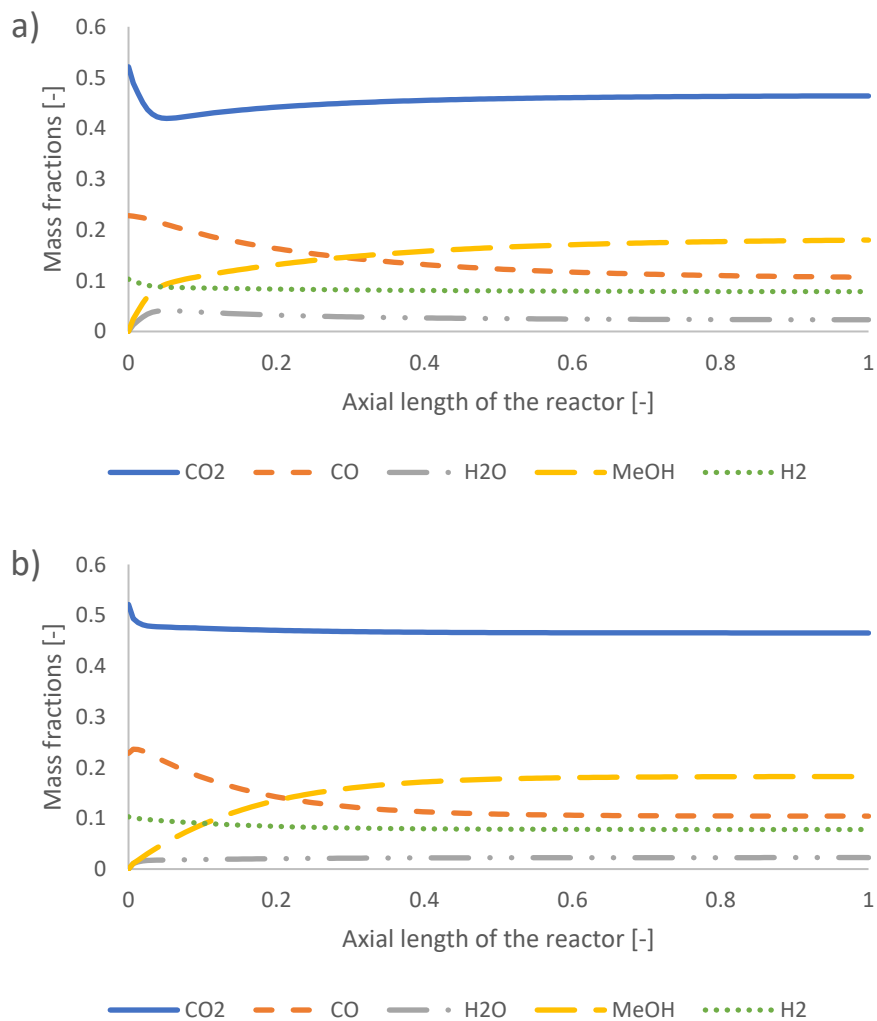


Figure A 7: Mass fractions of species along the axial direction (centreline) of the reactor for feed 14, predicted from a) Park's KM and b) Nestler's KM.

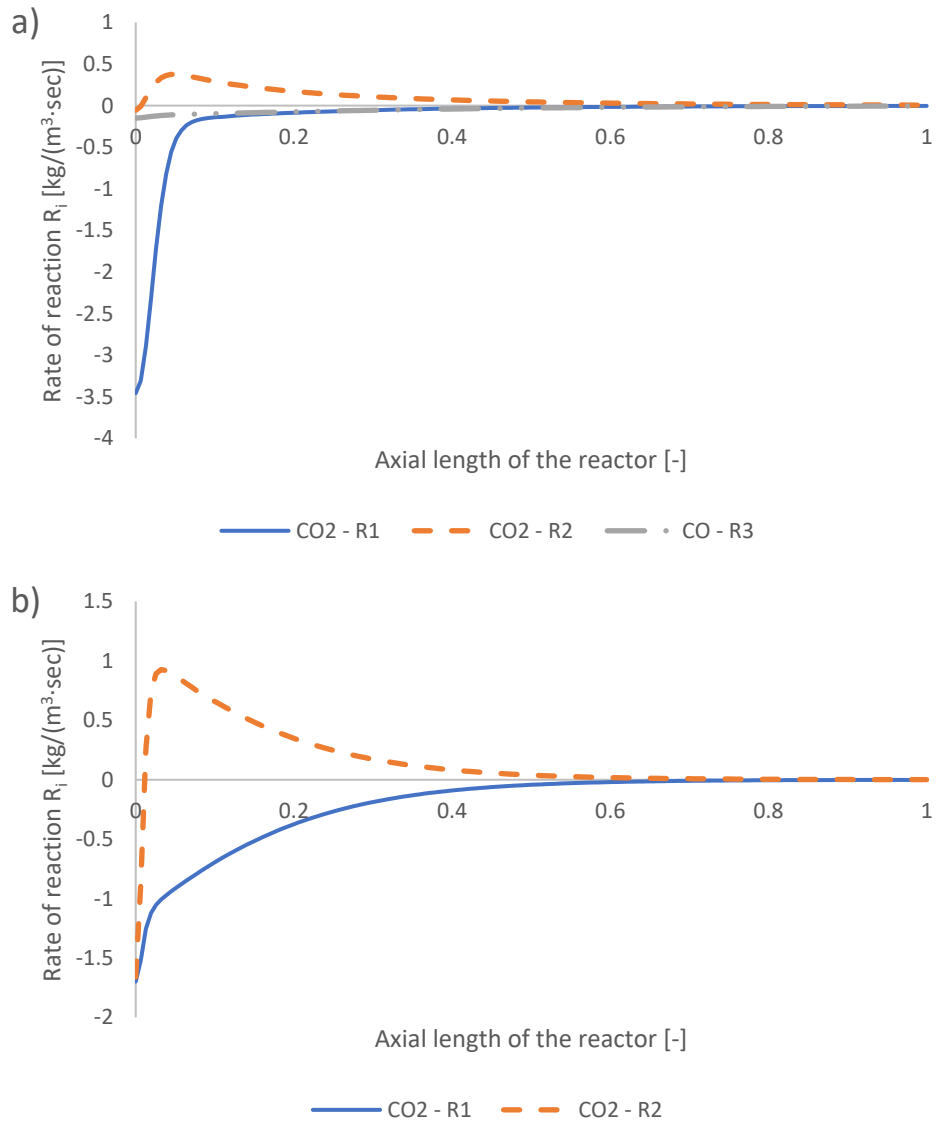


Figure A 8: Rate of reactions predicted from a) Park's KM for CO<sub>2</sub> (R<sub>1</sub> and R<sub>2</sub>) and for CO (R<sub>3</sub>) and from b) Nestler's KM for CO<sub>2</sub> (R<sub>1</sub> and R<sub>2</sub>).

Table A 6: Outlet species mass fractions for feed 14, predicted from the two kinetic models.

Feed 14 Species	Species outlet mass fractions	
	Park's KM	Nestler's KM
CO <sub>2</sub>	0.464	0.465
CO	0.107	0.104
H <sub>2</sub>	0.079	0.078
H <sub>2</sub> O	0.023	0.023
MeOH	0.180	0.182

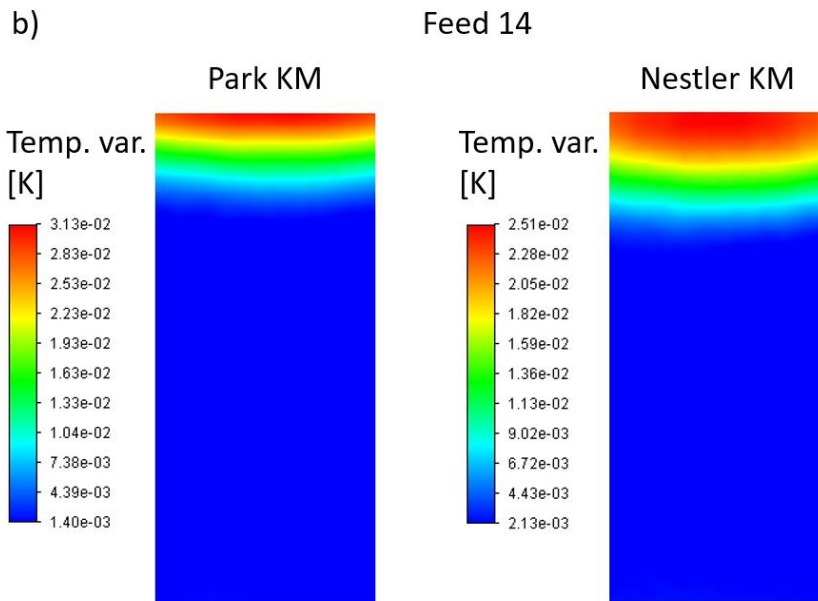
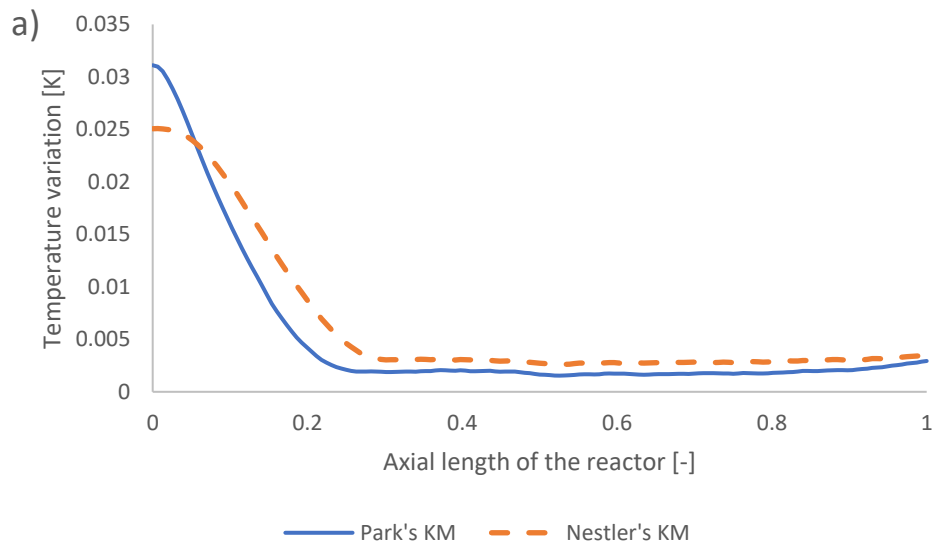


Figure A 9: Local temperature variation a) in the centreline of the reactor and b) along a 2D plane surface in the centre of the reactor, for feed 14, as predicted from the two KMs.

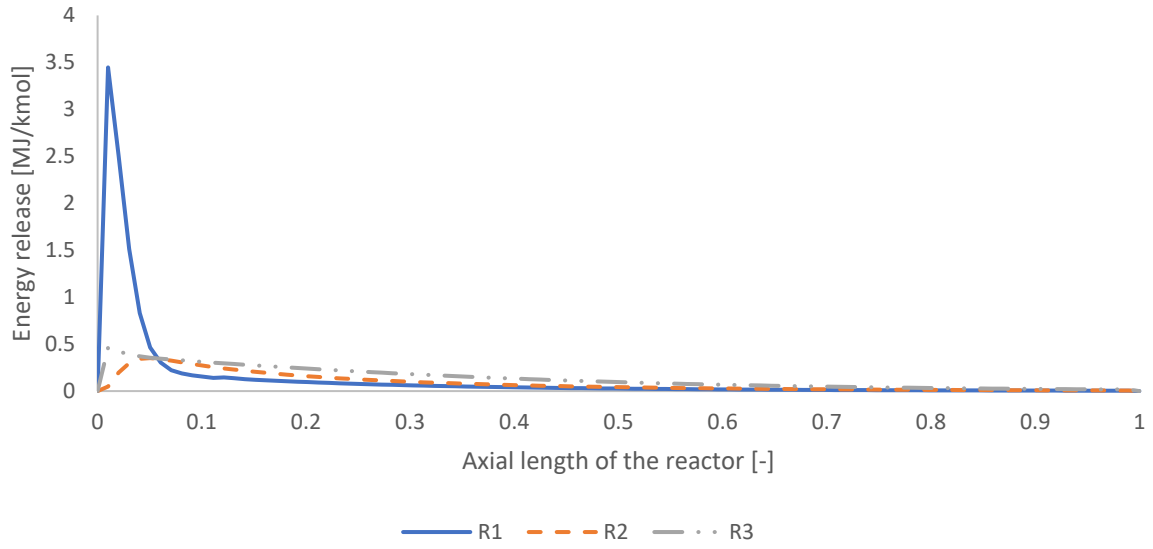


Figure A 10: Energy source or sink of reactions  $R_1$ ,  $R_2$ , and  $R_3$ , as predicted from Park's KM for feed 14.

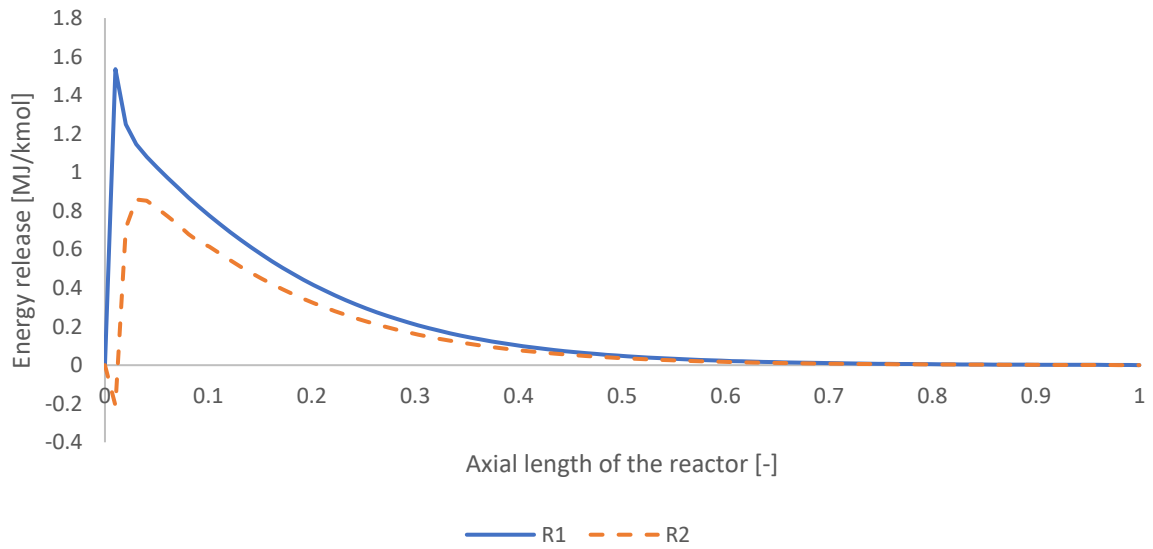


Figure A 11: Energy source or sink of reactions  $R_1$  and  $R_2$ , as predicted from Nestler's KM for feed 14.

## Feed 15

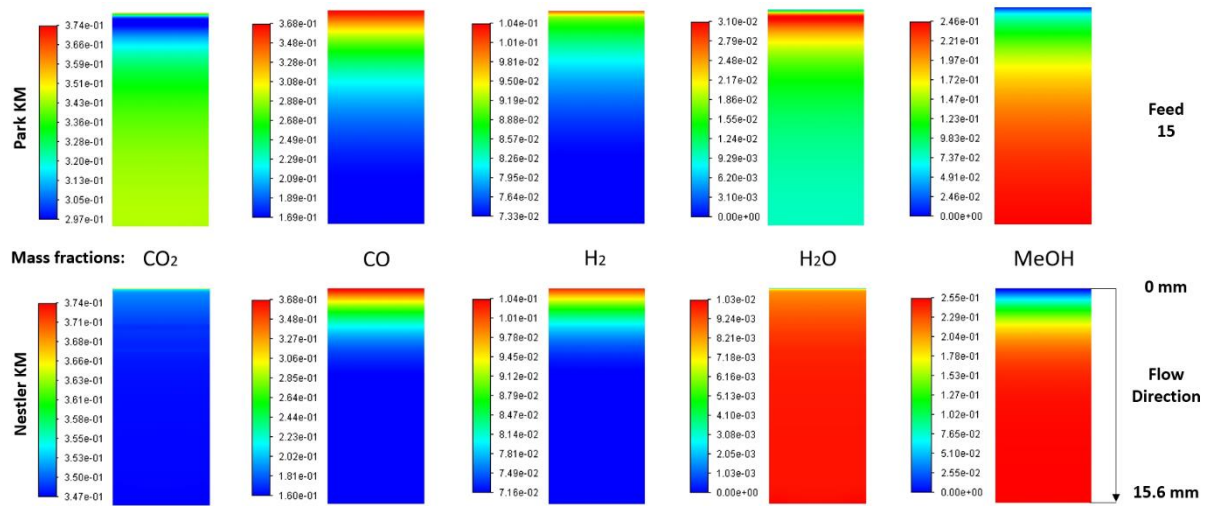


Figure A 12: Mass fractions of species along a 2D plane surface in the centre of the reactor for feed 15, predicted from both KMs.

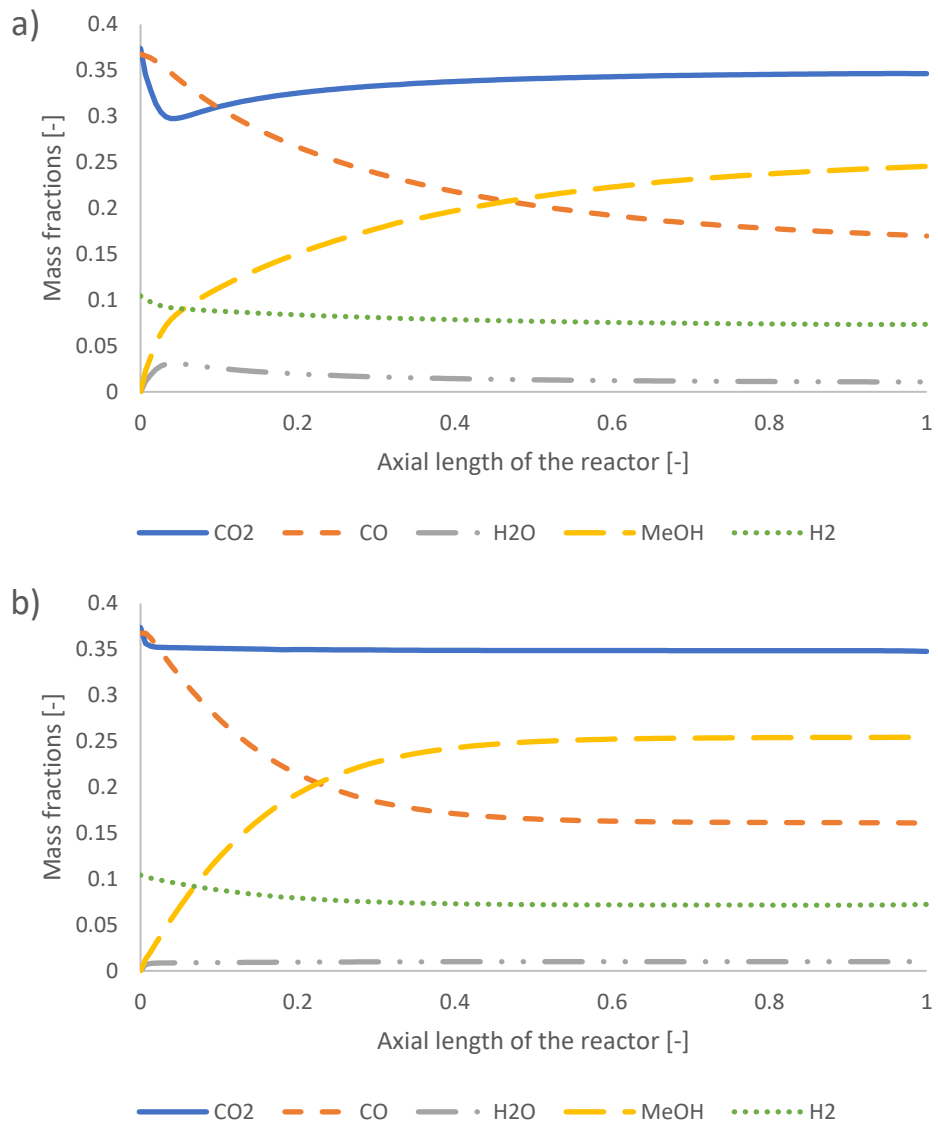


Figure A 13: Mass fractions of species along the axial direction (centreline) of the reactor for feed 15, predicted from a) Park's KM and b) Nestler's KM.

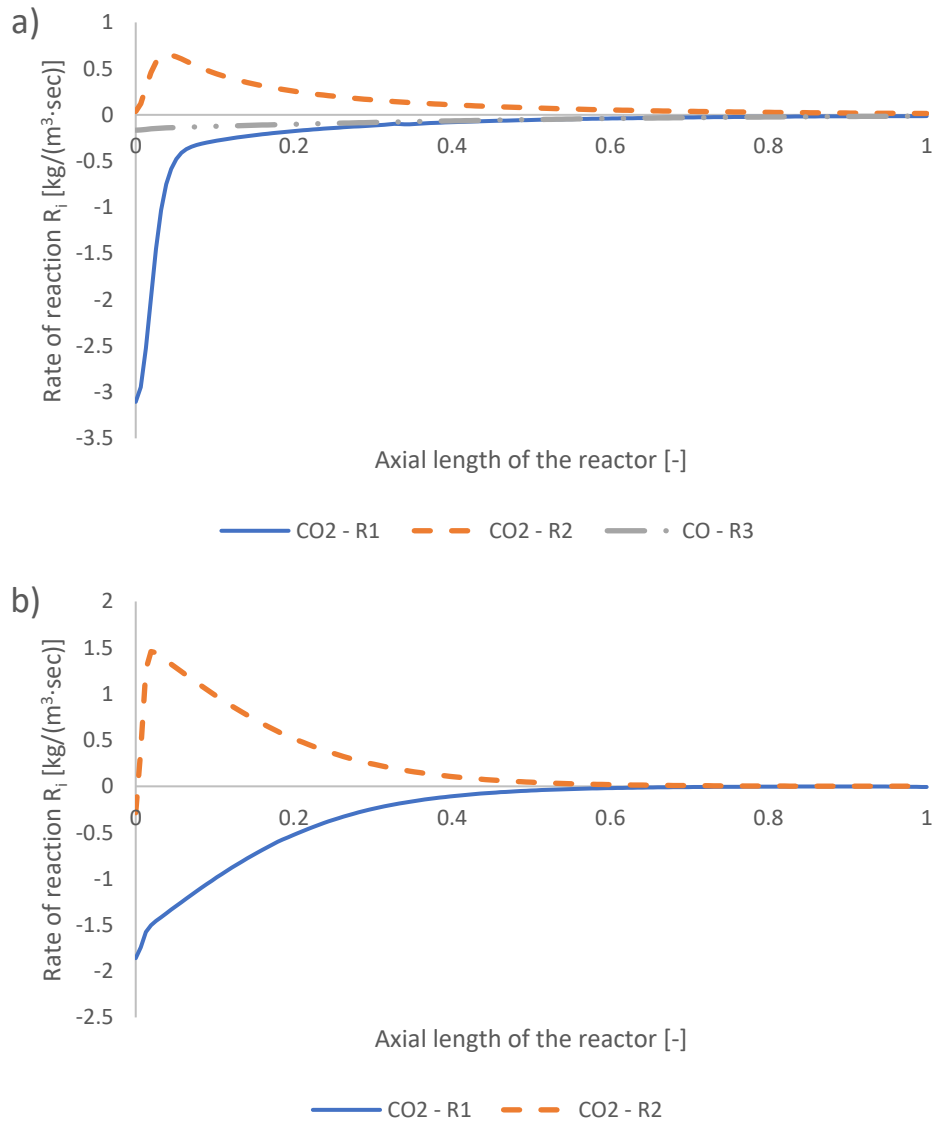


Figure A 14: Rate of reactions predicted from a) Park's KM for CO<sub>2</sub> (R<sub>1</sub> and R<sub>2</sub>) and for CO (R<sub>3</sub>) and from b) Nestler's KM for CO<sub>2</sub> (R<sub>1</sub> and R<sub>2</sub>).

Table A 7: Outlet species mass fractions for feed 15, predicted from the two kinetic models.

Feed 15 Species	Species outlet mass fractions	
	Park's KM	Nestler's KM
CO <sub>2</sub>	0.346	0.347
CO	0.169	0.160
H <sub>2</sub>	0.074	0.073
H <sub>2</sub> O	0.011	0.010
MeOH	0.246	0.255

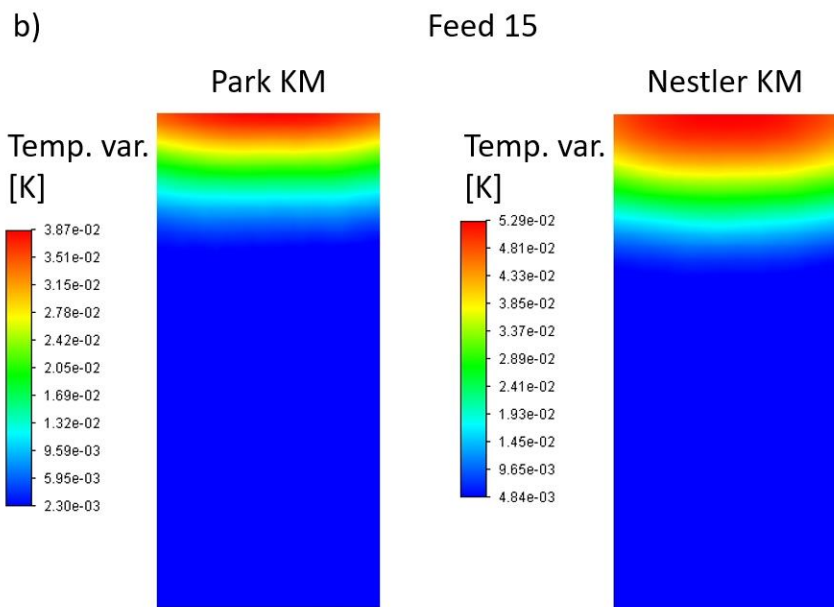
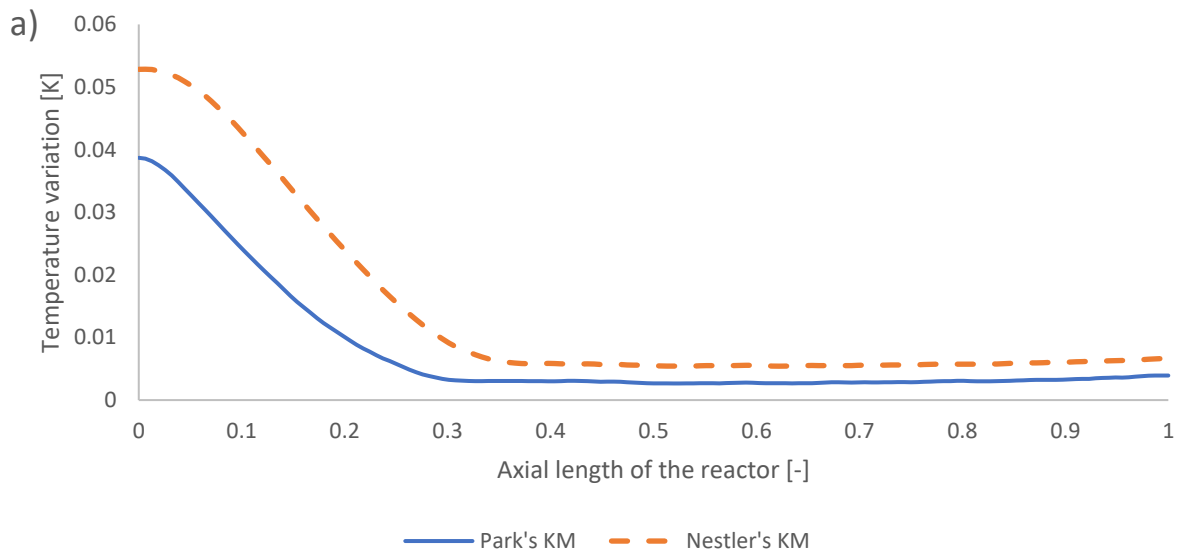


Figure A 15: Local temperature variation a) in the centreline of the reactor and b) in a 2D plane surface in the centre of the reactor for feed 15, as predicted from the two KMs.

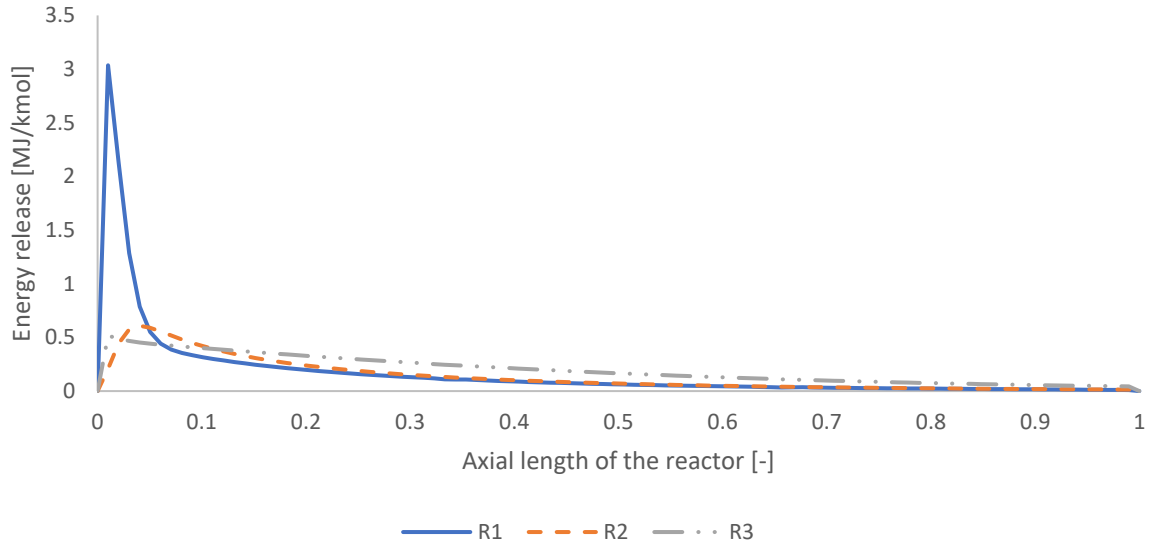


Figure A 16: Energy source or sink of reactions  $R_1$ ,  $R_2$ , and  $R_3$ , as predicted from Park's KM for feed 15.

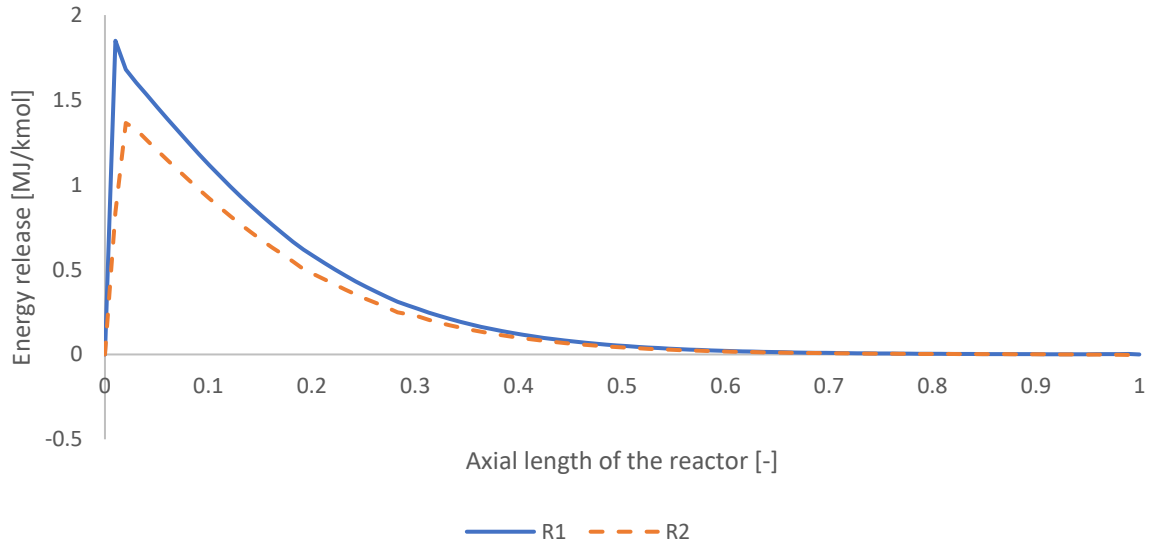


Figure A 17: Energy source or sink of reactions  $R_1$  and  $R_2$ , as predicted from Nestler's KM for feed 15.

## Feed 23

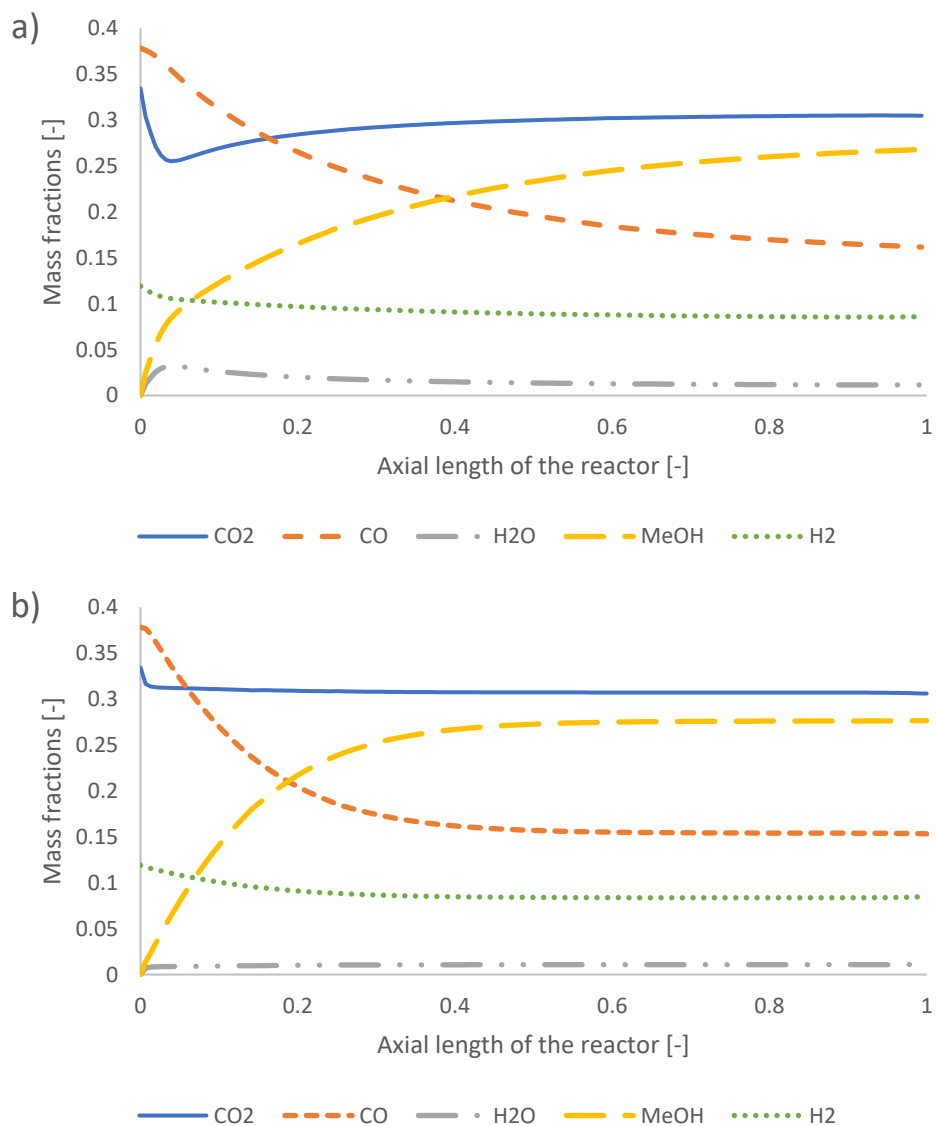


Figure A 18: Mass fractions of species along the axial direction (centreline) of the reactor for feed 23, predicted from a) Park's KM and b) Nestler's KM.

Table A 8: Outlet species mass fractions for feed 23, predicted from the two kinetic models.

Feed 23 Species	Species outlet mass fractions	
	Park's KM	Nestler's KM
CO <sub>2</sub>	0.304	0.305
CO	0.161	0.153
H <sub>2</sub>	0.086	0.085
H <sub>2</sub> O	0.012	0.011
MeOH	0.268	0.277

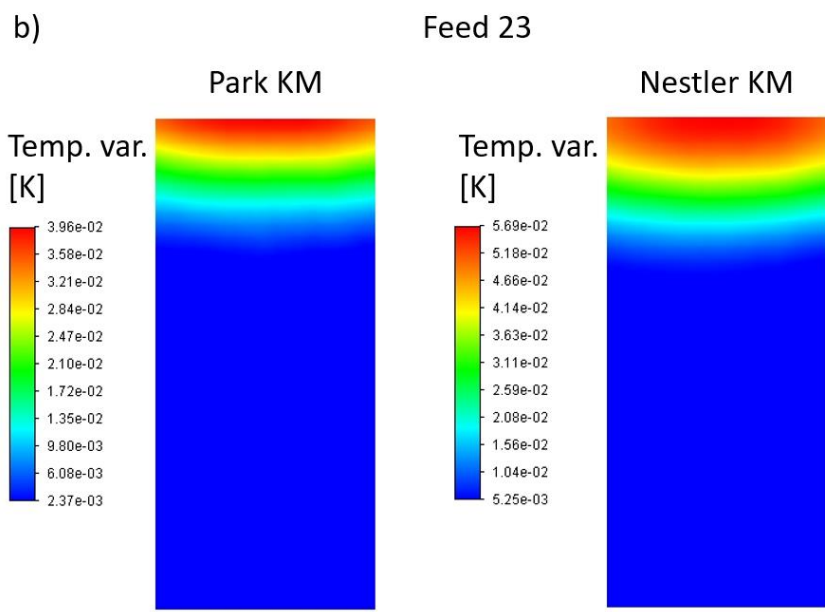
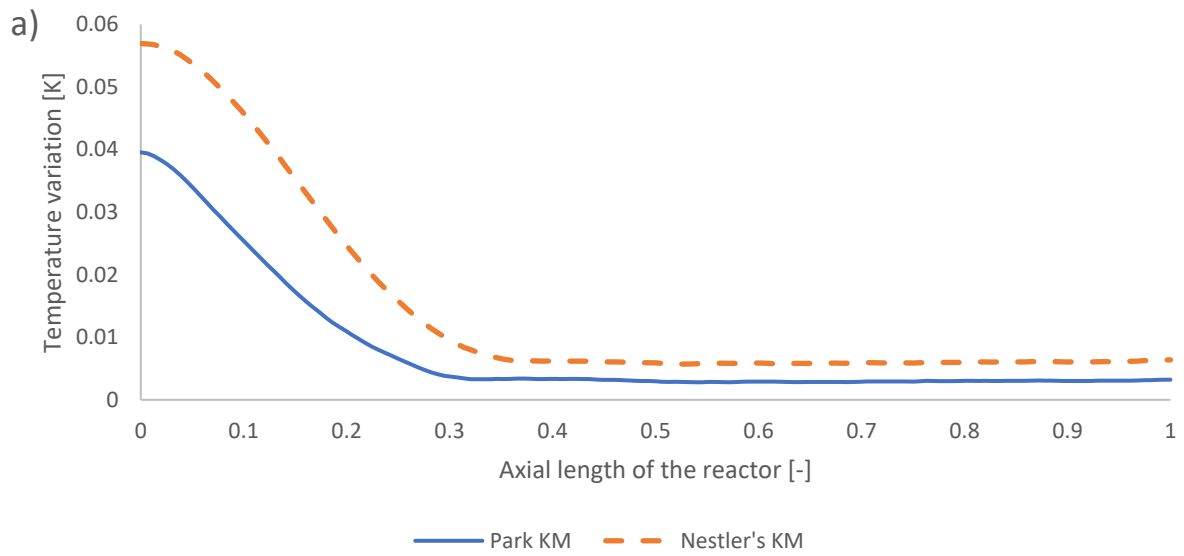


Figure A 19: Local temperature variation a) in the centreline of the reactor, and b) in a 2D plane surface along the centre of the reactor, for feed 23, as predicted from the two KMs.

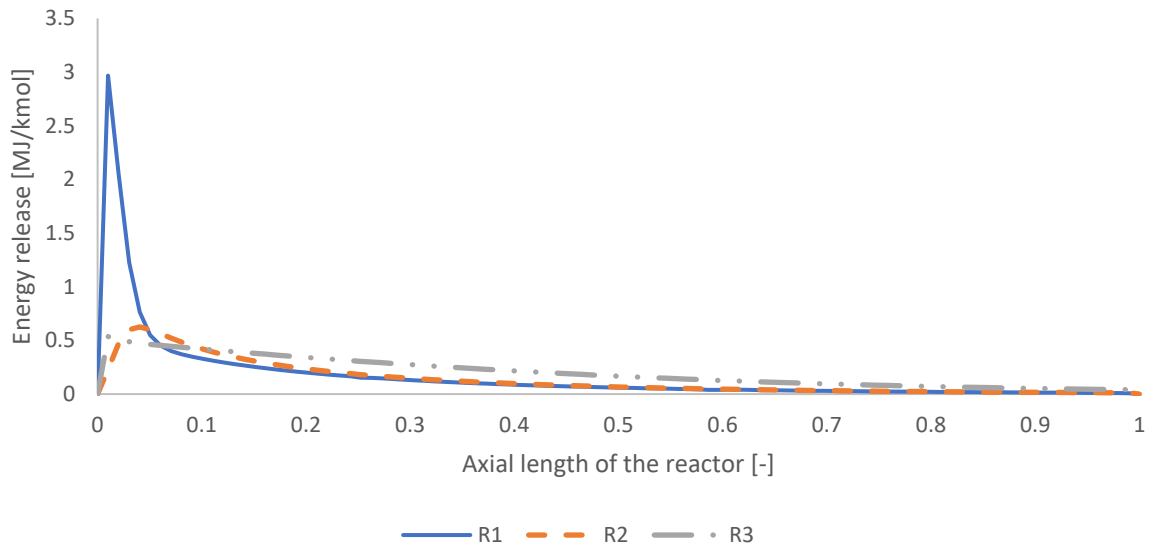


Figure A 20: Energy source or sink of reactions  $R_1$ ,  $R_2$ , and  $R_3$ , as predicted from Park's KM for feed 23.

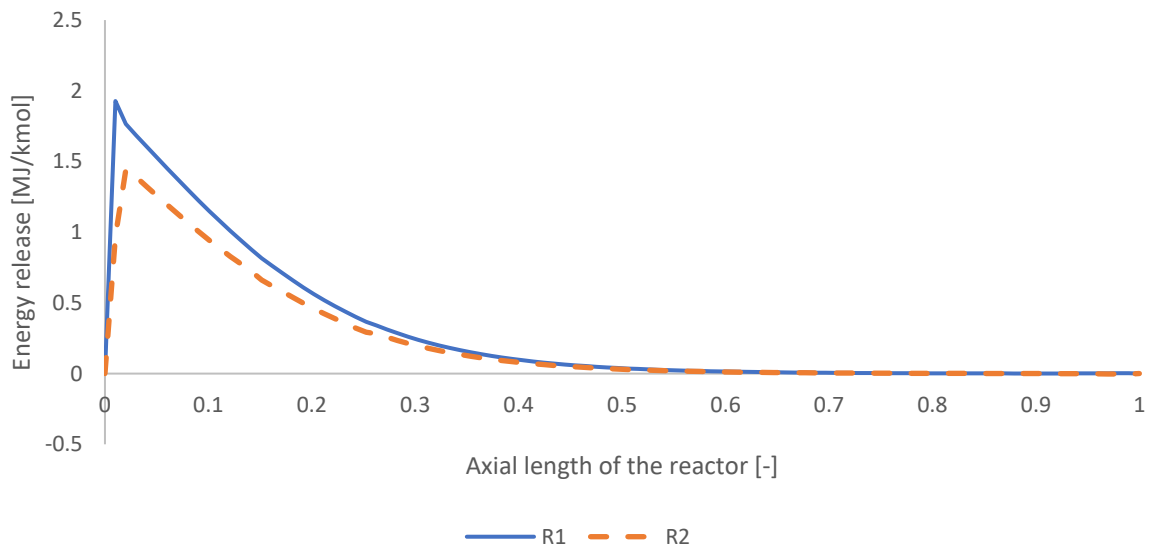


Figure A 21: Energy source or sink of reactions  $R_1$  and  $R_2$ , as predicted from Nestler's KM for feed 23.

## Feed 25

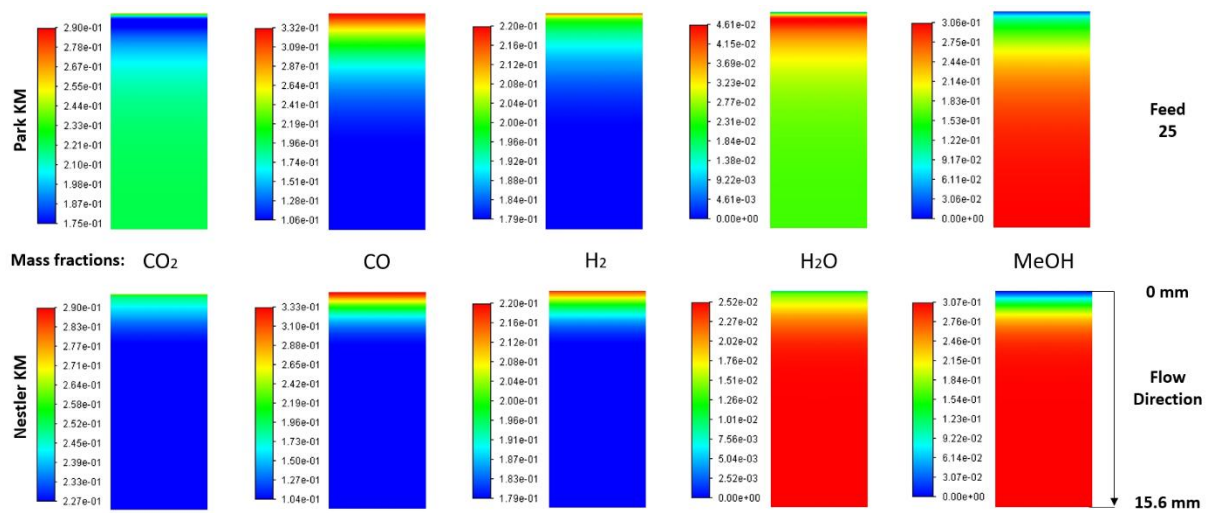


Figure A 22: Mass fractions of species along a 2D plane surface on the centre of the reactor for feed 25, predicted from both KMs.

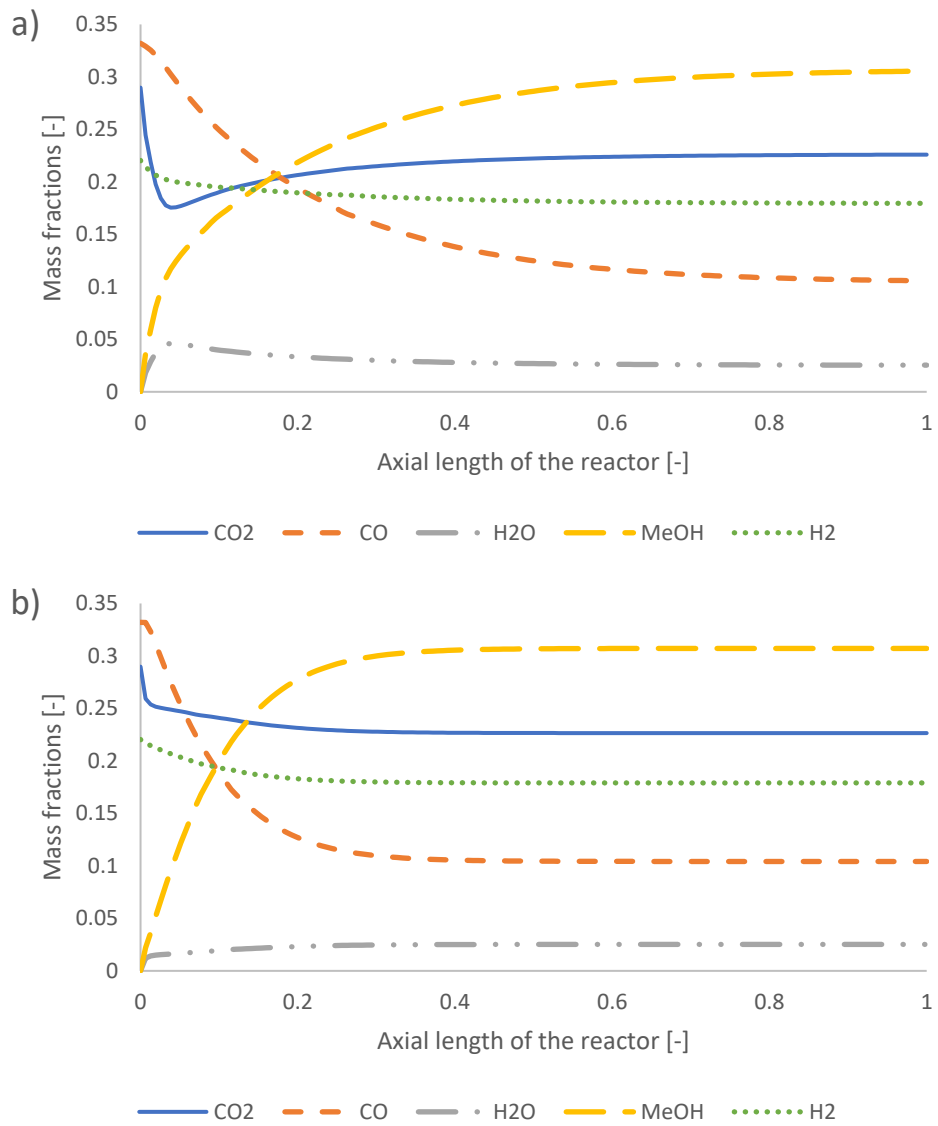


Figure A 23: Mass fraction of species along the axial direction (centreline) of the reactor for feed 25, predicted from a) Park's KM and b) Nestler's KM.

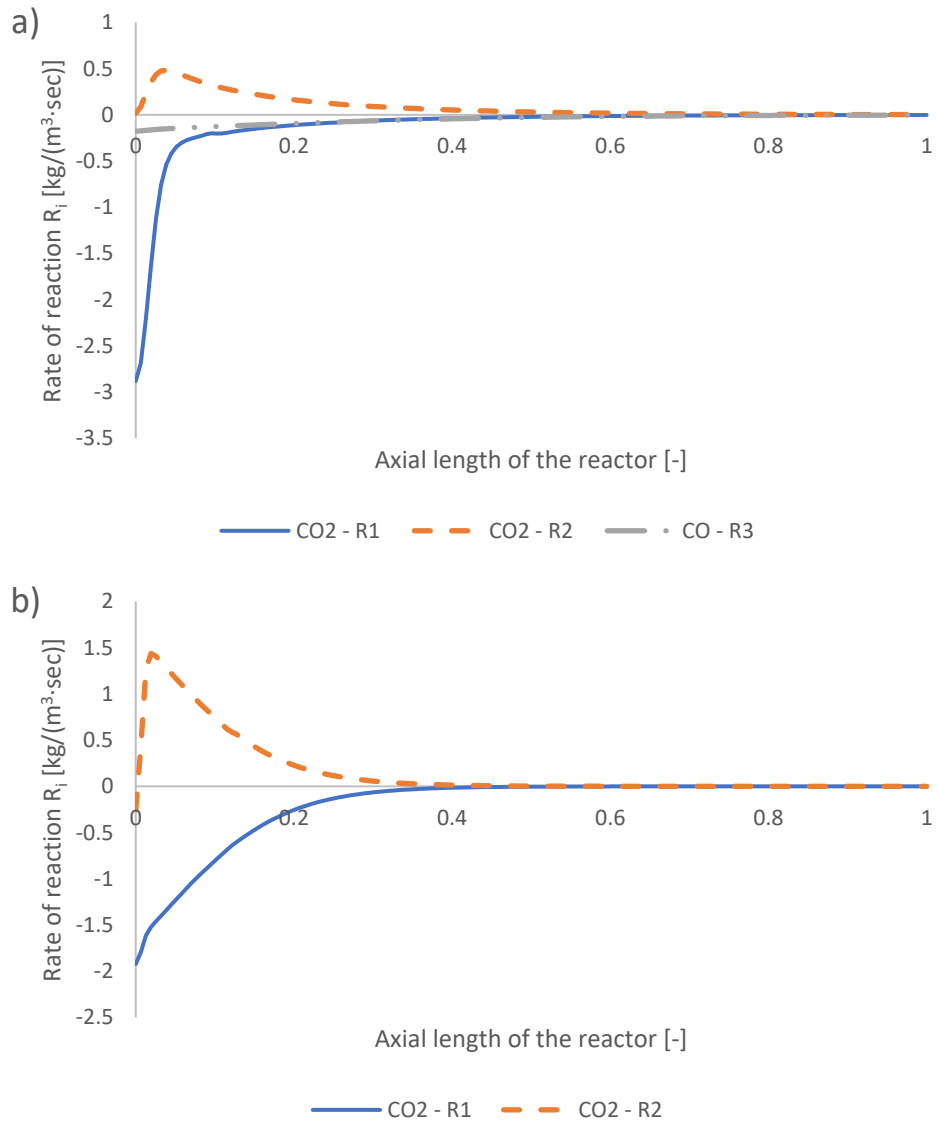


Figure A 24: Rate of reaction predicted from a) Park's KM for CO<sub>2</sub> ( $R_1$  and  $R_2$ ) and for CO ( $R_3$ ) and from b) Nestler's KM for CO<sub>2</sub> ( $R_1$  and  $R_2$ ).

Table A 9: Outlet species mass fractions for feed 25, predicted from the two kinetic models.

Feed 25 Species	Species outlet mass fractions	
	Park's KM	Nestler's KM
CO <sub>2</sub>	0.226	0.227
CO	0.106	0.104
H <sub>2</sub>	0.179	0.179
H <sub>2</sub> O	0.025	0.025
MeOH	0.306	0.307

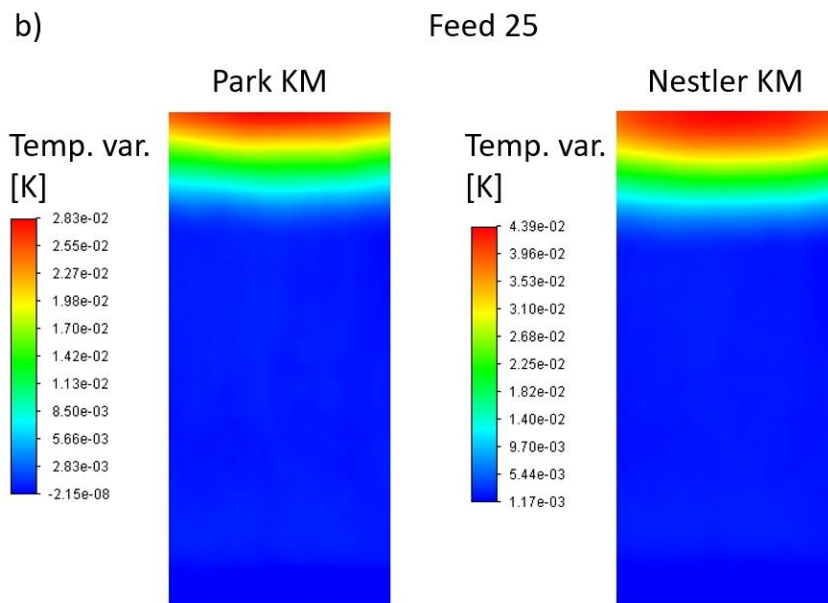
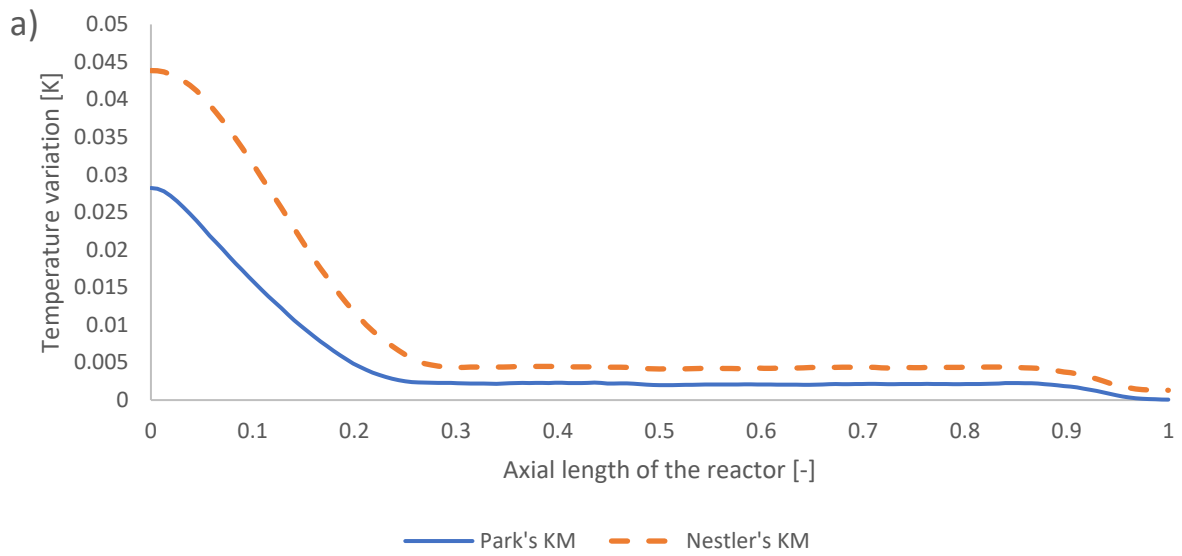


Figure A 25: Local temperature variation a) in the centreline of the reactor, and b) in a 2D plane surface along the centre of the reactor, for feed 25, as predicted from the two KMs.

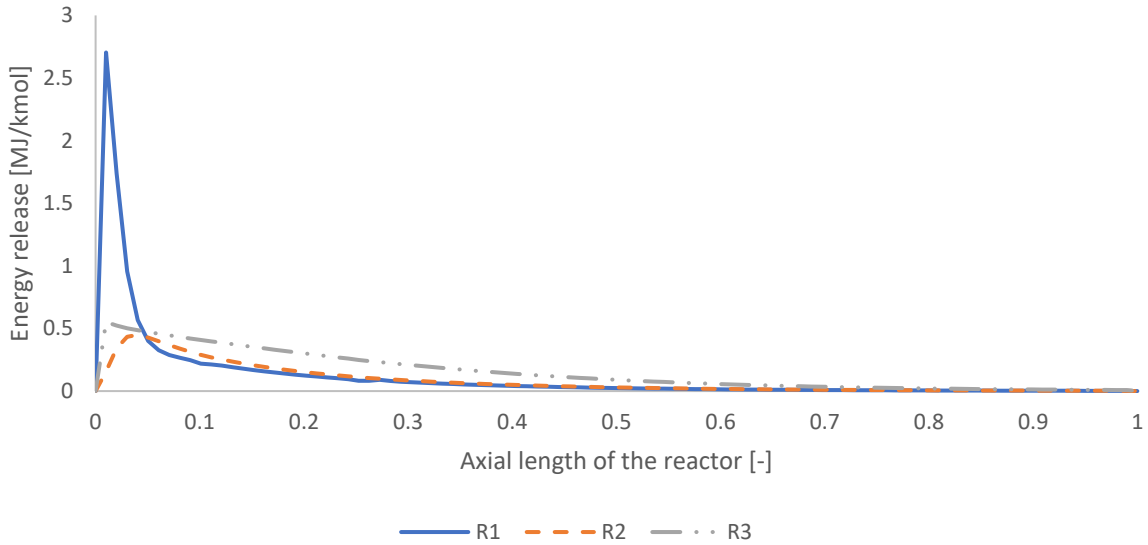


Figure A 26: Energy source or sink of reactions  $R_1$ ,  $R_2$ , and  $R_3$ , as predicted from Park's KM for feed 25.

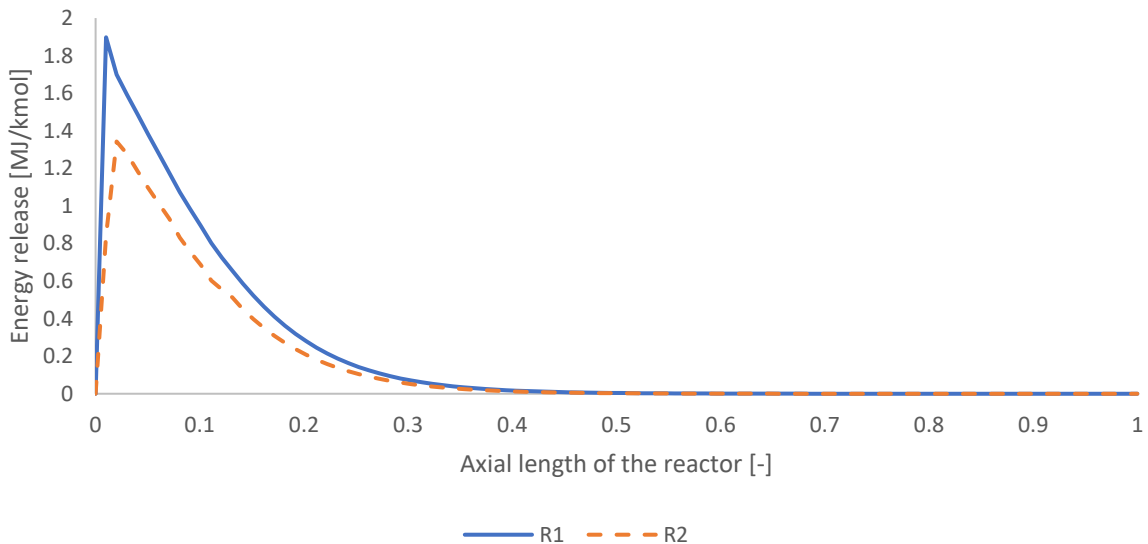


Figure A 27: Energy source or sink of reactions  $R_1$  and  $R_2$ , as predicted from Nestler's KM for feed 25.

## Grid dependency study

### Feed 23

As part of a grid independency study, coarser and more refined meshes were also investigated. This study is important for CFD models to identify the most adequate mesh size to reduce computational errors while also minimizing computational time requirement. The element sizes considered, along with the total mesh size and the error in the  $\text{CO}_2$  and  $\text{CO}$  outlet mass fraction predictions, for the kinetic model of Park and for feed 23, are presented in Table A 10. The 300k and 900k meshes are presented in Figure A 28. The mass fractions of  $\text{CO}_2$ ,  $\text{CO}$ ,  $\text{H}_2\text{O}$  and  $\text{MeOH}$ , along the centreline of the reactor for feed 23, for all available meshes, are presented in Figure A 29.

a)



b)

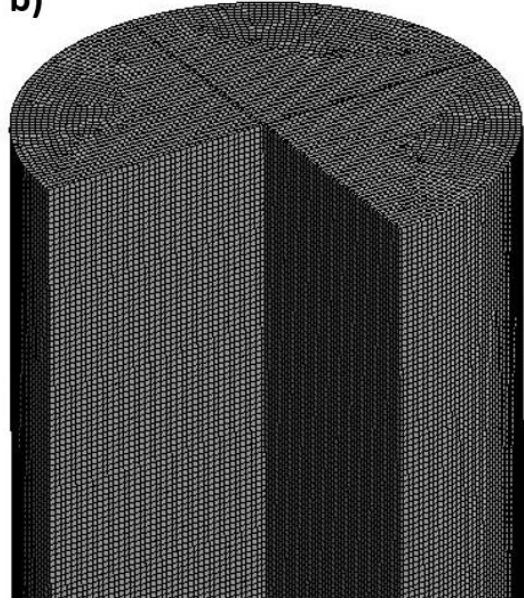
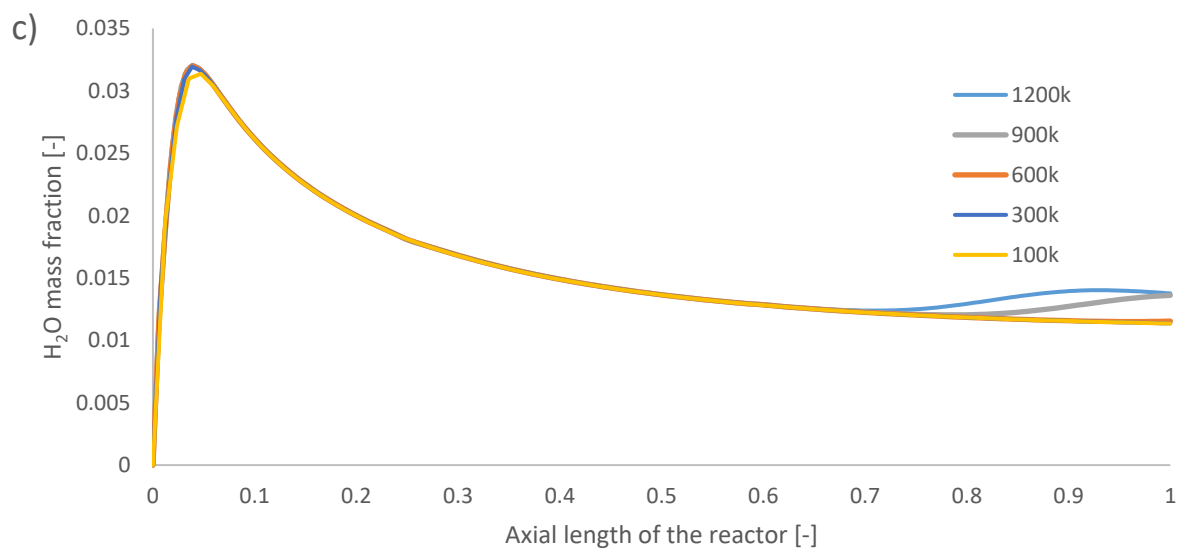
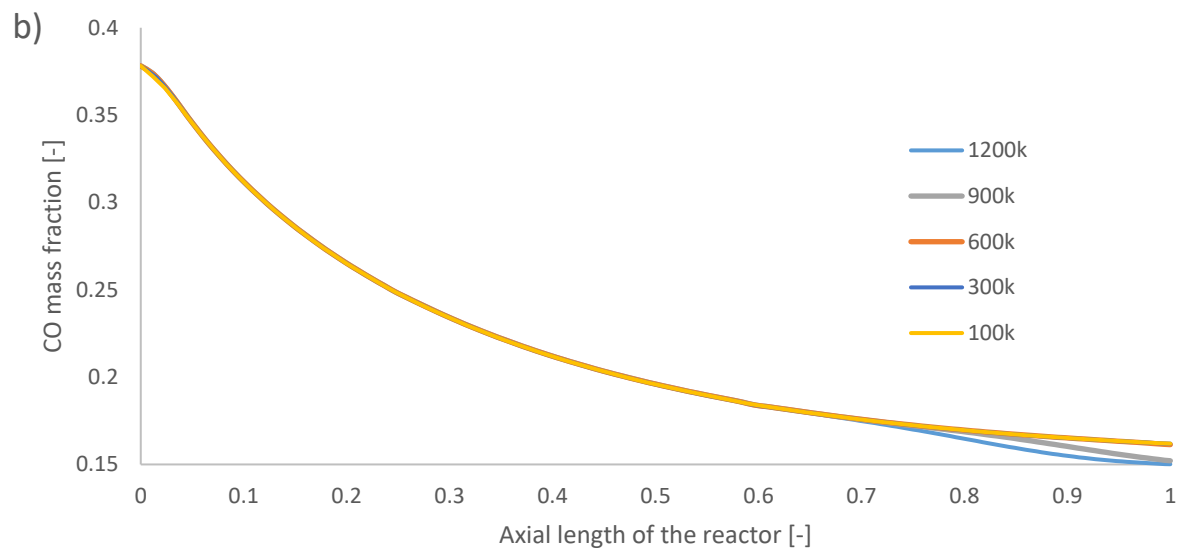
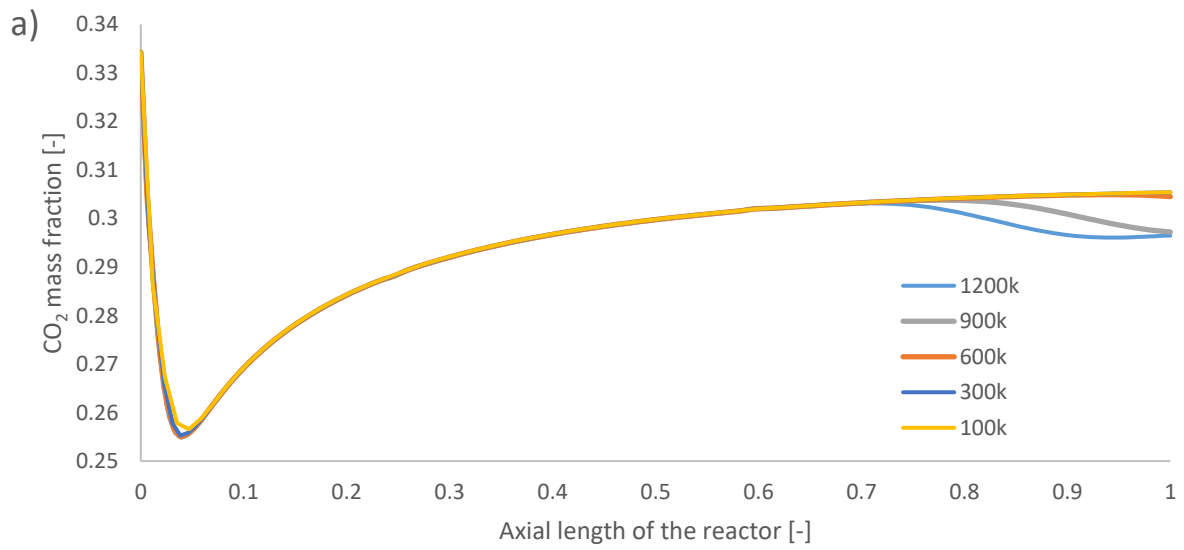


Figure A 28: a) 370 and b) 950 thousand elements mesh.



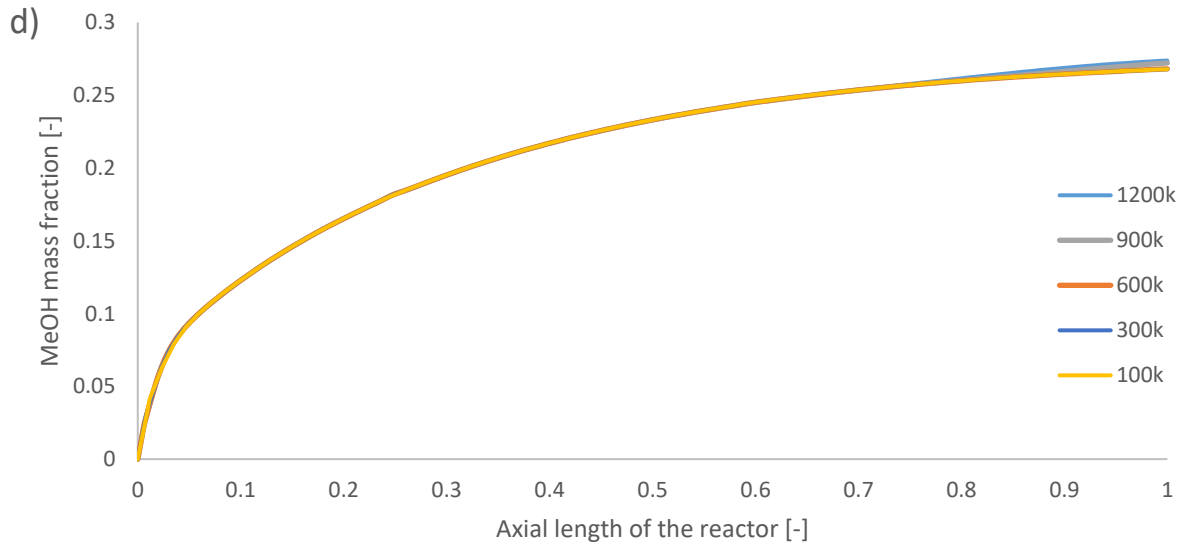


Figure A 29: Mass fraction of a) CO<sub>2</sub>, b) CO, c) H<sub>2</sub>O and d) MeOH along the centreline of the reactor for feed 23, produced from the three distinct meshes.

Table A 10: Mesh sizes, computational times, and predictions of Park's kinetic model for feed 23, as a result of the mesh independency study.

	Element Size [m]	Total Element count ( $\cdot 10^3$ ) [-]	Computational time [min]	Park's KM – Feed 23		
				CO <sub>2</sub> error [%]	CO error [%]	Collective error [%]
1200k	8e-5	1190	134	-3.60	-5.63	9.23
900k	8.7e-5	948	101	-3.35	-4.39	7.74
600k	1e-4	627	68	-1.08	1.23	2.31
300k	1.2e-4	370	39	-0.68	1.83	2.51
100k	1.85e-4	101	12	-0.67	1.85	2.52

For this study, the 600k mesh was chosen, as the collective CO<sub>2</sub> and CO errors, compared to the reported experimental mass fractions for feed 23, were the smallest among all five meshes, as seen in Table A 10. Yet, using the 300k mesh size instead would also be acceptable, as the species profiles are almost identical between the two cases.

### Feed 13

The mass fraction of CO<sub>2</sub> along the centreline of the reactor, for both kinetic models and for the five different mesh cases, are presented in Figure A 30. The comparative mass fraction of CO<sub>2</sub>, CO, H<sub>2</sub>O and MeOH along the axial direction, between the two kinetic models for feed 13 and for the mesh case of 600k, are presented in Figure A 31.

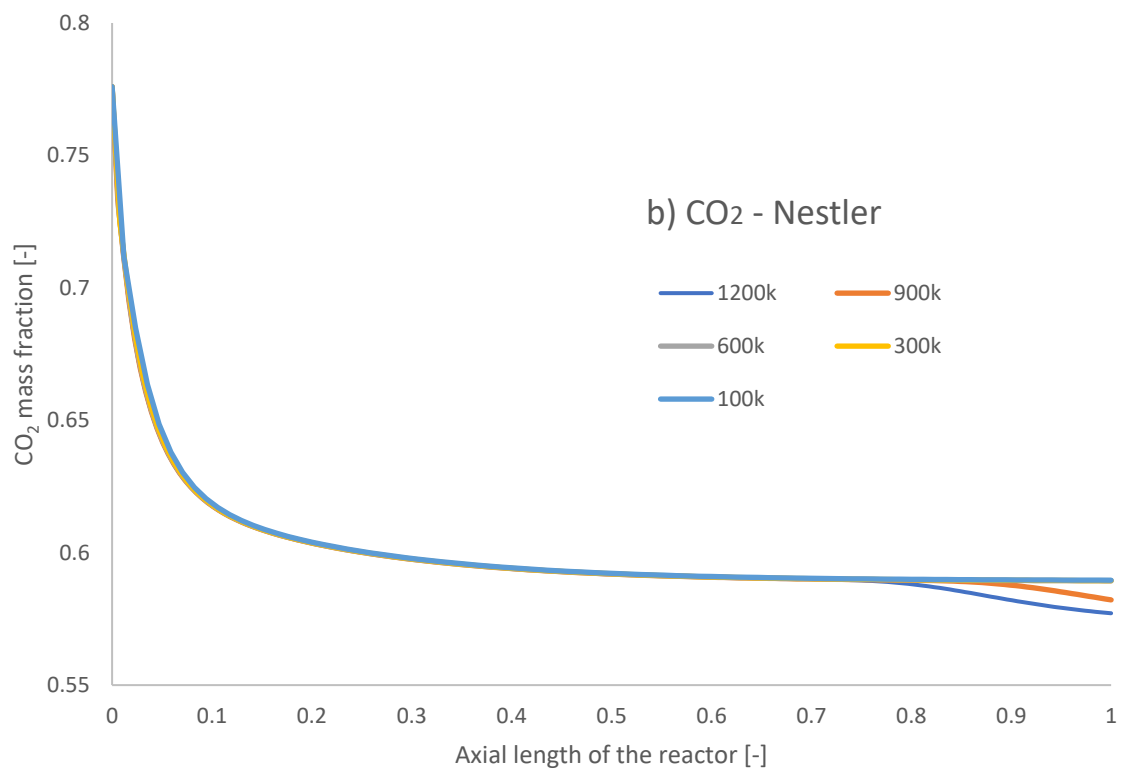
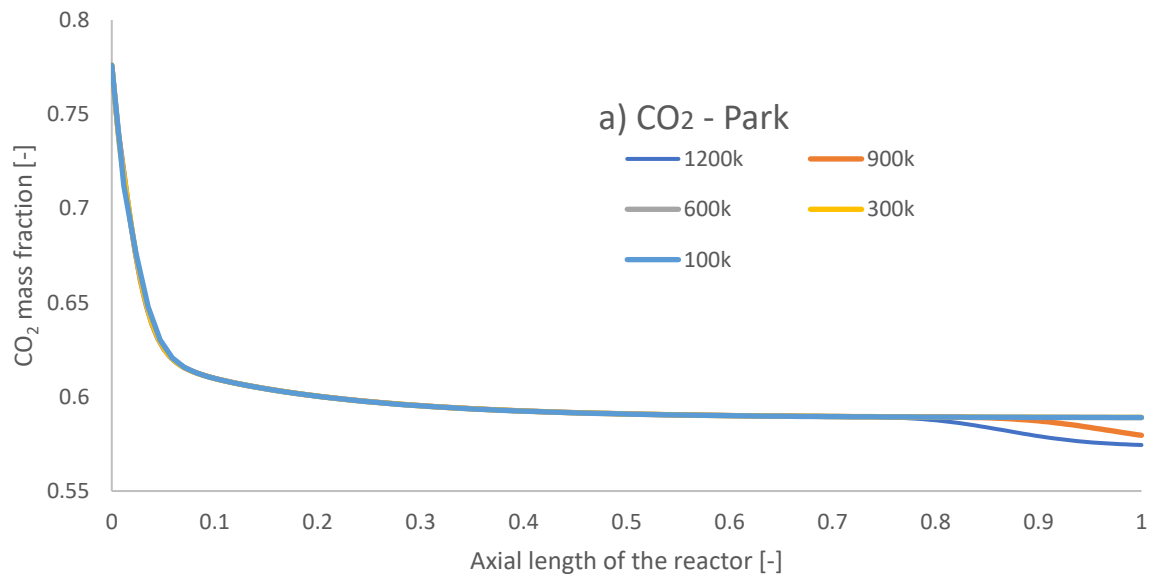
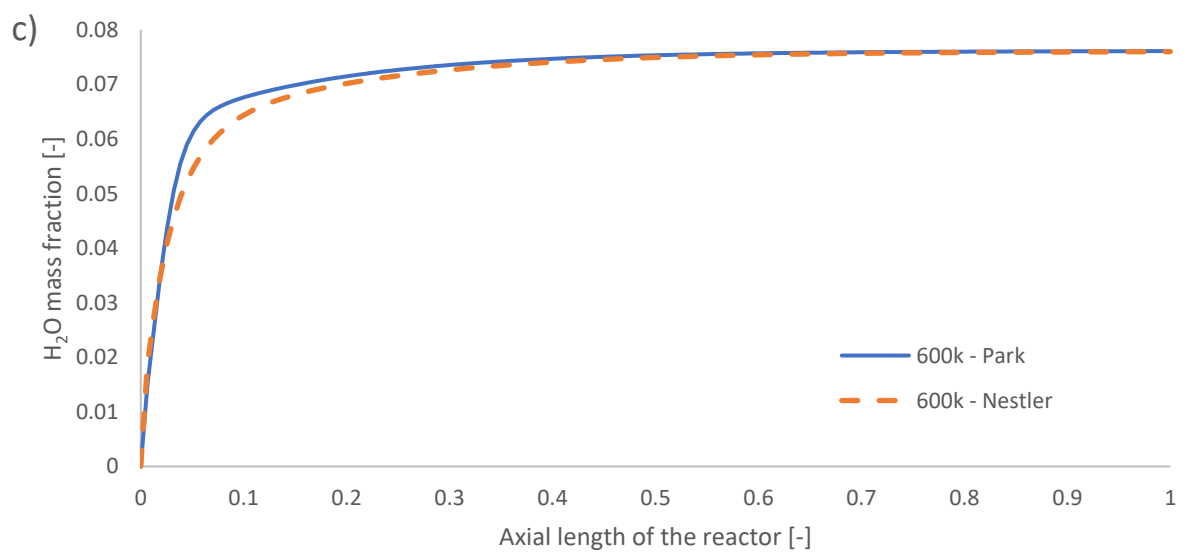
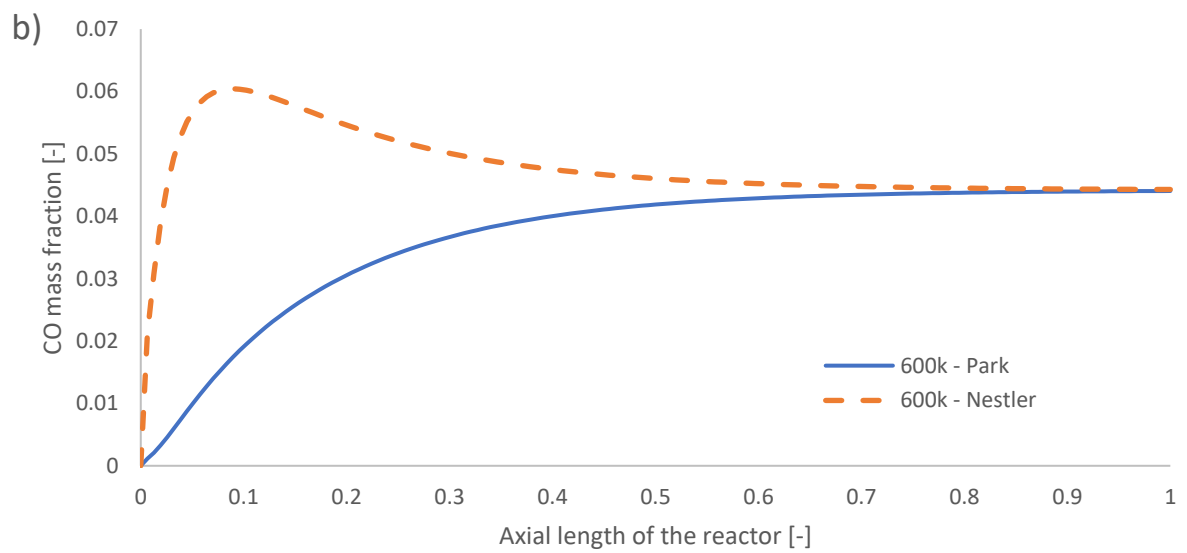
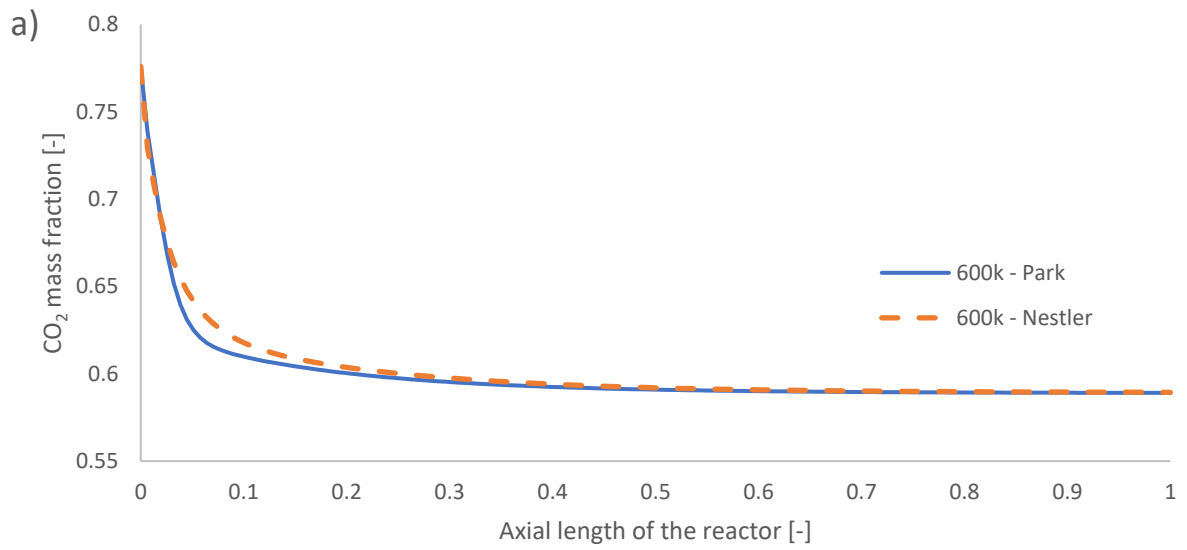


Figure A 30: Mass fractions of CO<sub>2</sub> along the axial direction for the different mesh cases, as predicted from a) Park's and b) Nestler's kinetic models.



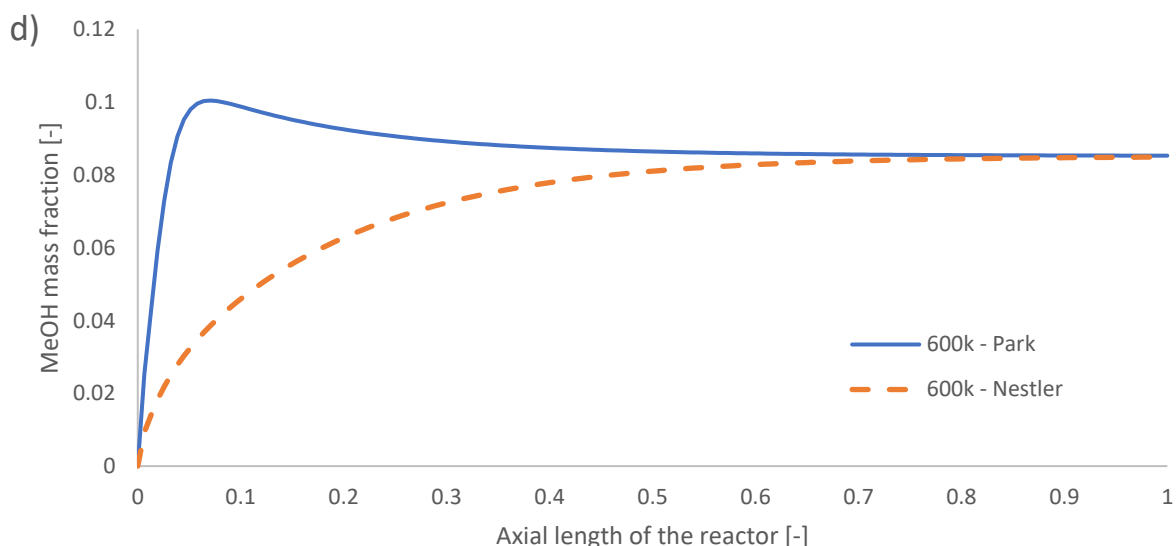


Figure A 31: Mass fractions of a) CO<sub>2</sub>, b) CO, c) H<sub>2</sub>O, and d) MeOH in the axial direction of the reactor, for feed 13 and for the 600k mesh.

### Backflow significance

In the most refined meshes, 900k and 1200k cases, and for both feeds, the mass fractions of CO<sub>2</sub>, CO and H<sub>2</sub>O near the outlet of the reactor suddenly change. A small variation near the outlet was also observed in the 600k mesh, yet compared to the 300k mesh, this increase was very small ( $\leq 0.3\%$ ). This mass fraction change does not have a physical meaning, but instead is caused as a result of backflow, i.e. reversed flow, at the outlet boundary of the reactor. To get an estimate of the magnitude of this variation, the mass fractions of species on the axial distances of 0.9 and 1.0 were investigated for the 600k mesh case and for both kinetic models. For this investigation, the species mass fractions of all five feeds (feeds 13, 14, 15, 23, and 25), were considered. In some cases, the species mass fractions have not reached a steady state by the outlet, e.g. feed 13 of Nestler's KM (Figure A 2) or feeds 15 and 23 of Park's KM (Figure A 13 and Figure A 18, respectively). These local mass fraction changes are the result of reaction rates rather than backflow, and thus were not considered for the estimate. In the remaining cases, mass fraction changes are only caused by backflow of species, and in average across all feeds and both kinetic models, this local variation is below  $\leq 0.2\%$ . Conclusively, the impact of any backflow in the 600k mesh can be considered negligible; the penetration of backflow in the catalyst volume is limited only in the near-outlet region (up to a maximum of 0.9 axial length) and thus will not affect the flow profile within the main catalytic body.

The reverse flow introduces additional species, thus changing the local concentration of the nearby computational elements. As the species conservation equation, eq. ( 8 ), is dependent on this local concentration through the term  $\nabla\varphi^i$ , these additional backflow species negatively impact the conservation equation and result in computational errors. The finer the mesh, the higher the number of local elements affected by this backflow, and thus the deeper the penetration of backflow errors within the bed.

Backflow of species can be caused by different reasons, some of which are poor mesh quality, incorrect boundary conditions, or short downstream length. Regarding the mesh quality, for the 600k case, the orthogonal quality and the skewness of the mesh elements is 0.99 and 0.07, with the ideal values for them being 1.0 and 0.0, respectively. Orthogonal quality refers to the local topology of the mesh elements, while skewness is the difference of the shape of the cell and the shape of an

equilateral cell of equivalent volume (2). These values indicate that the mesh quality is very good and therefore it is not the reason for the backflow. Similarly, boundary conditions can also be excluded as the cause of the backflow; all cases, for all feeds and both kinetic models, are modelled with the same pressure outlet, yet only some of these cases present backflow effects at the 600k mesh. This means that most probably the main reason for the backflow is short downstream length. The available cases have different setups for the flow, i.e. inlet species concentration or inlet flow velocity, which also results in a unique flow field each time. After leaving the outlet, the flow needs additional space to equalize, which the current geometry does not account for. Unfortunately, this lack of space in the outlet results in an unsteady flow and recirculation effects. The recirculation effect can explain the temperature drop observed in Figure A 25; as both the mass fractions and the reaction rate magnitudes have both reached a steady-state by the outlet, the temperature drop can only be the result of a cooling recirculating flow.

Improvements in the geometry can help reduce the backflow impact; specifically, the usual method, also used by Dixon (6), is the expansion of the geometry at the outlet with an unreactive zone to allow enough space for the flow to equalize. It should be mentioned that this flow improvement methodology mainly applies to small recirculation effects in the near-outlet region, as is the 600k case. It does not apply to cases where the numerical errors are inherently caused by the kinetic model, as is the case with feed 13 using Nestler's kinetic model (Fig. 6 of the main paper).

## References

1. Park N, Park M-J, Lee Y-J, Ha K-S, Jun K-W. Kinetic modeling of methanol synthesis over commercial catalysts based on three-site adsorption. *Fuel Processing Technology*. 2014;125:139-47.
2. ANSYS Inc. ANSYS Fluent Theory Guide. 2013;Release 15.0.
3. ANSYS Inc. ANSYS Fluent User's Guide. 2013;Release 15.0.
4. Nestler F, Schütze AR, Ouda M, Hadrich MJ, Schaadt A, Bajohr S, et al. Kinetic modelling of methanol synthesis over commercial catalysts: A critical assessment. *Chemical Engineering Journal*. 2020;394:124881.
5. Achenbach E. Heat and flow characteristics of packed beds. *Experimental Thermal and Fluid Science*. 1995;10(1):17-27.
6. Dixon AG. Local transport and reaction rates in a fixed bed reactor tube: Endothermic steam methane reforming. *Chemical Engineering Science*. 2017;168:156-77.
7. Taskin ME, Troupel A, Dixon AG, Nijemeisland M, Stitt EH. Flow, Transport, and Reaction Interactions for Cylindrical Particles With Strongly Endothermic Reactions. *Industrial & Engineering Chemistry Research*. 2010;49(19):9026-37.
8. Dixon AG, Taskin ME, Nijemeisland M, Stitt EH. CFD Method To Couple Three-Dimensional Transport and Reaction inside Catalyst Particles to the Fixed Bed Flow Field. *Industrial & Engineering Chemistry Research*. 2010;49(19):9012-25.
9. Hite RH, Jackson R. Pressure gradients in porous catalyst pellets in the intermediate diffusion regime. *Chemical Engineering Science*. 1977;32(7):703-9.
10. Fuller EN, Schettler PD, Giddings JC. NEW METHOD FOR PREDICTION OF BINARY GAS-PHASE DIFFUSION COEFFICIENTS. *Industrial & Engineering Chemistry*. 1966;58(5):18-27.
11. Krishna R. Problems and pitfalls in the use of the Fick formulation for intraparticle diffusion. *Chemical Engineering Science*. 1993;48(5):845-61.
12. Poling EB, Prausnitz MJ, O'Connell PJ. *Properties of Gases and Liquids*, Fifth Edition. 5th ed. New York: McGraw-Hill Education; 2001.
13. Graaf GH, Scholtens H, Stamhuis EJ, Beenackers AACM. Intra-particle diffusion limitations in low-pressure methanol synthesis. *Chemical Engineering Science*. 1990;45(4):773-83.
14. Beeckman JW. Mathematical description of heterogeneous materials. *Chemical Engineering Science*. 1990;45(8):2603-10.

15. Ghanbarian B, Hunt AG, Ewing RP, Sahimi M. Tortuosity in Porous Media: A Critical Review. *Soil Science Society of America Journal*. 2013;77(5):1461-77.
16. Son M, Woo Y, Kwak G, Lee Y-J, Park M-J. CFD modeling of a compact reactor for methanol synthesis: Maximizing productivity with increased thermal controllability. *International Journal of Heat and Mass Transfer*. 2019;145:118776.
17. Graaf GH, Winkelman JGM. Chemical Equilibria in Methanol Synthesis Including the Water–Gas Shift Reaction: A Critical Reassessment. *Industrial & Engineering Chemistry Research*. 2016;55(20):5854-64.